Utrecht University

Faculty of Geosciences
Master in Water Science and Management

Fluvial flood risk: an inundation modelling study to analyze the contribution of river embankments to flood risk downstream

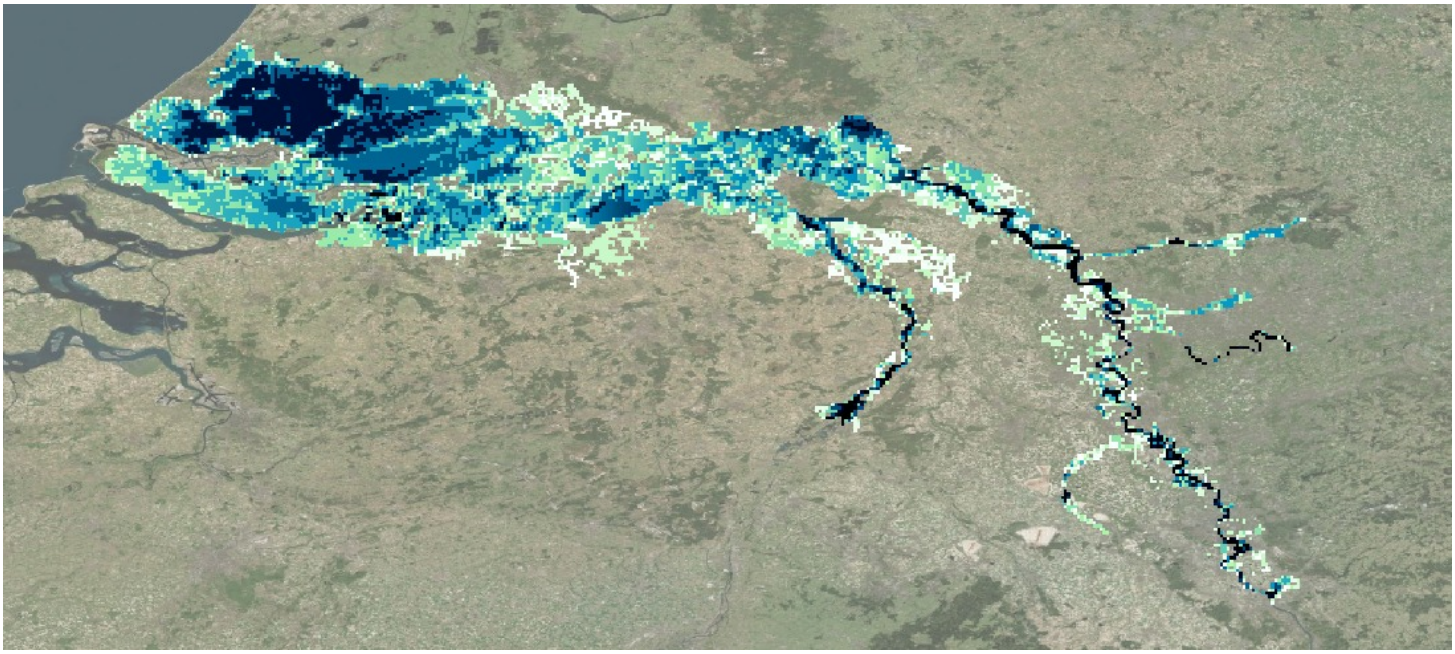

Supervisor:
Dr. Rens van Beek

Second Reader:
Prof. dr. Hans Middelkoop

Student
Pietro Stradiotti (6563554)
p.stradiotti@students.uu.nl

A master thesis submitted in partial fulfillment of the requirements for the degree of Master programme in Water Science and Management in the Faculty of Geosciences at Utrecht University.

Acknowledgments

A much needed thanks to Rens for supervising my work and being always there to help. A heartfelt thanks goes also to Timothy for his supervision, which I never gave for granted, and Philip for welcoming me six months ago and providing me with the ideas and supervision for the thesis.

My deepest gratitude and affection also go to Jinmoo for having shared all the moments of this work and having supported me all the way through, as only a real 불알친구 could do.

Infine, grazie dal profondo del cuore a Giulia per i preziosissimi consigli e per essersi appassionata al mio lavoro. Una scusa a mamma e papà per tutto il tempo che non ci siamo potuti vedere, ed un grazie per l'impagabile supporto che non mi fate mai mancare.

Summary

One very effective way to protect a settlement from river flooding has been traditionally to build embankments along the river channel and prevent the flood wave from entering the floodplain. However, the very mechanism that works for protection, by constraining the water in the channel, causes a shift of hazard further downstream in the river, as demonstrated by observations of increase in the flood frequency and magnitude downstream of embankments. The framework of risk can be used to quantify this effect and form a basis for the reassessment of this type of flood protection measure. To this purpose, the present study develops a scenario-based analysis to evaluate the effect of design protection levels on the expected annual damage (EAD) in the catchment at the level of embankments and downstream. The methodology developed is based on the use of the existing framework for integrated flood modelling GLOFRIM, which couples the capacities of the well-known hydrological model PCR-GLOBWB and hydrodynamic model Lisflood FP. Using this setup, the flood hazard is mapped and used to build exceedance probability-loss (EPL) curves for the catchment on the basis of distributed exposure and vulnerability data. From these curves, the EAD can be retrieved and compared for each scenario. The findings of the study for the region of the Niederrhein evidence that the risk of flood increases as the protection level upstream becomes higher. The magnitude of this effect is found to be in the order of an overall increase of 0.9 – 1.7 billion $ for the whole catchment, which is significant event when compared to the effect of climatic projections. This study also represents a proof of concept and a call to include this effect on large-scale risk assessment models, to reach a deeper-level analysis, furthering our accuracy in representing risk at the regional- and global-scale.

Table of Contents

Word count: 12967

1. Introduction

The aim of this chapter is to provide the context of the research and to introduce the notions which are necessary to understand the following sections. First, the elements leading to the definition of the research problem are laid out, after which the objective and research questions are stated. After this, the theory of the concepts introduced is explained. Finally, the societal and scientific relevance of the research is argued.

1.1. Subject definition

Riverine flood events are tragically familiar to most societies across the globe on the human time scale, their adverse effects ranging from nuisances to catastrophes depending on the loss of lives and properties involved. The concept of risk grasps this interaction, using a probabilistic approach to characterize the potential damage that may occur in a place as result of a particular event. Humans take on a significant role in amplifying the risk of floods on many levels, one of which is the increase of exposure and vulnerability (Ceola et al., 2014). This occurs for instance in developing contexts, when informal settlements in flood-prone cities are overpopulated by people seeking better living conditions (Braun & Aßheuer, 2011). Countries where flood management is approached more systematically, such as the Netherlands, suffer from the same trends as economic development increases the value of assets already at risk (De Moel et al., 2011). Risk also increases by magnification of the hazard, which occurs when land-use change upstream affects the hydrological regime of a catchment (Hounkpè et al., 2019), or indirectly as the global hydrological cycle is subject to the effects of climate change (Alfieri et al., 2017). Therefore, a critical step to promote adaptation and achieve a positive interaction of humans with floods is to unravel the complexity of the role they play in increasing risk.

One way humans have traditionally acted on fluvial flood risk is through the implementation of flood protection measures (White, 1945). Engineering works have been put in place to manipulate the course and morphology of rivers and reduce the local hazard, by constraining, diverting and facilitating the transfer of the flood wave so that the volume of water is safely moved downstream. Measures of this type include the channelization and straightening of the riverbed, meander cut-offs and confinement of the flow through dikes and embankments. The latter especially have fulfilled a primary role in flood defence. Features such as the relative ease of construction and apparent sense of safety have ensured an extensive use of river embankments, evocatively defined as a 'levee love affair' (Tobin, 1995). However, a new vision of catchment-based holistic management (WMI, 2004) has called into question the downsides relative to their interaction with the hydrological fluvial regime that follows their use. In particular, an aspect of focus of their critics has been the response of downstream flood conditions to their presence. The latter aspect will be the focus in the following discussion.

1.1.1. River embankments and flood dynamics

To conceptualise the embankment-inundation interplay, the starting point is to investigate what effect is produced on river flow. As a matter of fact, flood control is in large part focussed on this specific aspect

(Yen, 1995). For this reason, it has been vital for authors to develop a general theory of flow under the presence of embankments as a base for strategic flood management. Such theory is articulated in studies based on historical observations, computer modelling and hydraulic conceptual models. The latter can to a certain extent offer a concise understanding of the effects of embankments on the river flow and flood conditions. A key work is the one of Yen (1995), who attempted to develop a theoretical model of this interaction by considering the energy and flow continuity equations along a schematic river reach. The author found for the section downstream of the levees that, with respect to a condition of levee absence, the rating curve of the river was lowered. This means that for a same discharge value, the depth of water in the channel will be smaller (Figure 1). However, this conclusion is limited to an ideal condition of steady uniform flow, and departs from the complexity and specificity of real flow conditions (Yen, 1995).

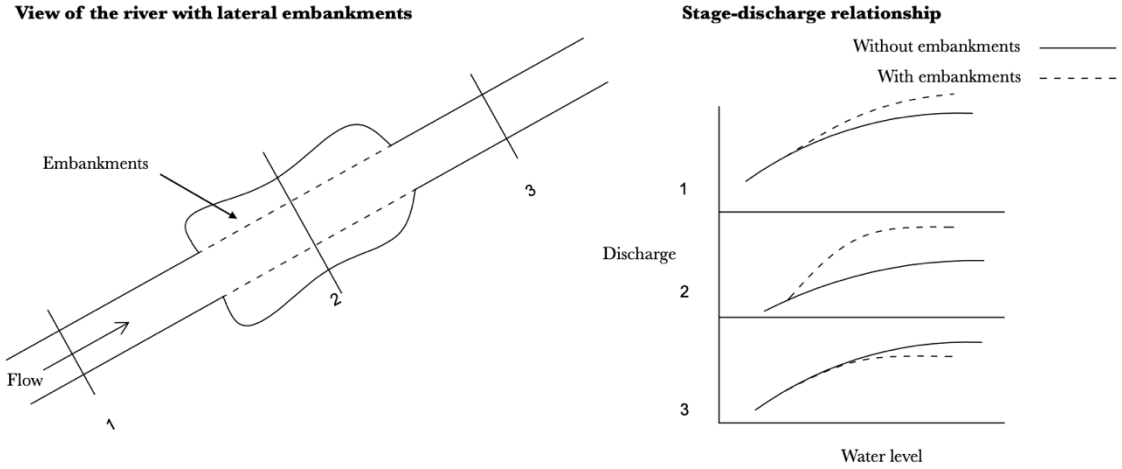

Figure 1: Hydraulic effect of levees on the discharge-stage relationship of a simplified river reach. Adapted from Yen (1995).

In a real catchment the effect of river embankments is very much dependent on their spatial configuration and the contextual river characteristics, such as morphology and hydrological flow conditions. For instance, Sanyal (2017) argues that embankments along rivers are in most cases not uniformly distributed but rather scattered along the river course, as consequence of 'ad hoc' protection designs. Failing to provide a spatially integrated protection might have a hydraulic result in the accentuation of the likelihood of overbank flow in the area downstream of a dike segment, producing the opposite of what would be the desired effect (Sanyal, 2017). On a larger catchment scale, the interaction becomes even more complex, as the impact of river embankment is not limited to the local hydraulics, but also on the overall loss of storage volume which is taken up in the floodplain. In fact, while fulfilling their function of constraining the flood wave in the channel, river embankments prevent the spill of flood water in the near floodplain, thereby reducing its water retention capacity. The latter plays a crucial role in dampening the flood wave, allowing to flatten the discharge curve by 'topping off' the peak. Previous studies have positively correlated the floodplain to a reduction of the peak discharge downstream during flood events (Lammersen et al., 2002). As a proof of concept, Heine & Pinter (2012) reported that the

river stage downstream was observed to lower after events that provoked upstream embankment breach for a few locations in the Mississippi river. This is evidence of the fact that if the water is allowed to pour out in the place where the dike is built, the pressure that otherwise builds up downstream during extreme events is alleviated. Instead, when dikes are built along a reach, the contribution of the water drained in the channel is not set off by overbank spillages and adds up to the flood wave, which can only accumulate and recur larger in volume downstream (Tobin, 1995). Moreover, with embankments preventing water retention, the response of the basin produces less attenuation of the hydrograph while it is routed downstream, resulting in a sharper peak discharge (Clilverd et al., 2016) (Figure 2). Therefore, the mechanism that makes embankments effective, by preventing overbank flow in the protected area, tends to reproduce and aggravate the risk for the remaining of the routing path.

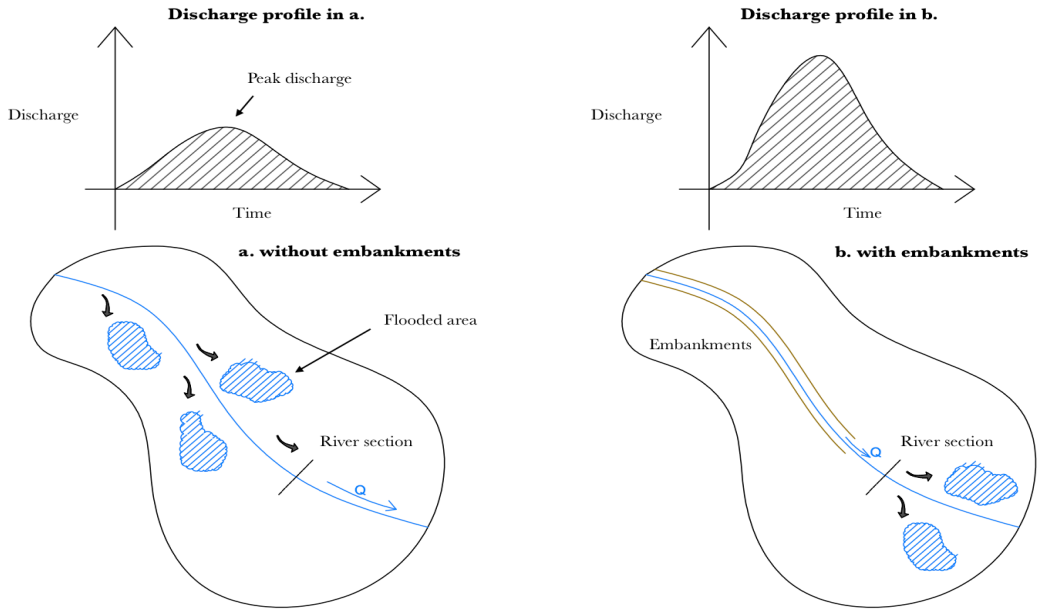

Figure 2: (simplified) effect of embankments on flood propagation in a catchment. The graphs represent a schematic flood hydrograph at the river section (author's own).

The magnification of flood downstream of river embankments has been proved across a variety of case studies. A study of the Missouri and Mississippi rivers by Criss & Shock (2001) found that after major engineering works of dike construction and channelization, a steady increase of the flood stage at constant discharge has occurred for the downstream catchment area. Furthermore, the recurrence interval for major floods has been observed to shorten, making them more frequent and suggesting an increase in flood hazard downstream. Similarly, embankments along the Po river were imputed as flood-contributing factors for the downstream floodplain because of the effect produced on the flood wave propagation. In this case, Di Baldassarre et al., (2009) were able to prove that the discharge peak downstream was heightened by the effect of dikes in extreme floods. While this effect is not evident at normal flows, rare events such as 500-year return period floods are predicted to produce a more severe repercussion in terms of the associated damage (Di Baldassarre et al., 2009). In the Vietnamese Mekong river, where the development of high dikes has changed the hydrodynamics of the region, this contributed to prolonged flood duration, higher peak flood levels and 30 to 80% of the flood level increase downstream (Thanh et al., 2020; Triet et al.,

2017). Arguably, the use of embankments as river flood protection measure prioritizes a defence in loco over preserving a balance in the upstream-downstream flood dynamics, often creating the conditions for flood magnification and shifting the hazard from the protected area further downstream. The gradual resort to this measure for different basins worldwide over increasing sections of the river courses has aggravated this problem, by installing a locked-in mechanism where the outcomes of previous interventions create more issues and call for more interventions. In the cornerstone of socio-hydrology, Di Baldassarre et al. (2013) have efficaciously demonstrated how measures taken at presence and on the basis of current conditions alone might worsen the negative consequences of floods in the future. In addition to this temporal disconnection, an upstream-downstream inconsistency in flood management could prove a hindrance towards achieving fully integrated flood control at the catchment level.

1.1.2. Research problem

River embankments are simple engineering solutions that find extensive application globally. Nevertheless, their interaction with the hydrodynamic behaviour of rivers is complex and does not limit to offer flood safety in the protected areas. Instead, as proven for cases in the most diverse contexts, it changes the hydrological balance of a catchment and promotes the condition for flood aggravation downstream. For this reason, communities that take up riparian areas downstream of embanked rivers may experience an increase of inundation risk. Previous research has focused primarily on the effect of embankments on rivers using historical data analyses (Criss & Shock, 2001; Pinter et al., 2008) and hydrodynamic modelling of the river (Di Baldassarre et al., 2009; Thanh et al., 2020; Sanyal, 2017), basing the comparison on the hydrological regimes prior and after their construction. An increase of flood risk will follow these hydrological changes, posing a threat to the very presence and prosperity of societies downstream of embanked river sections. Risk is the concept that connects the purely hydrological aspects of this issue to the sphere of decision-making, on the governmental, societal and private level, because it can be valued in monetary terms (Botzen & van den Bergh, 2012) and hence become a leverage for political decisions in flood management. Flood risk has to be recognised in order to attribute responsibility, raise awareness in the public and in the governmental spheres, as well as achieve an attitudinal change to address the issue (Treby et al., 2006). The aspect of risk for the issue at hand has been generally overlooked, as the current understanding lacks an analysis of flood risk change in the catchment due to the presence of embankments.

The research aims to increase our understanding of the interaction between embankments and upstream-downstream flood dynamics using the framework of risk. To this purpose, hydrological and damage modelling will be applied on a catchment to evaluate flood risk under the assumption of different protection scenarios. The objective is to quantify the change in risk experienced by the upstream and downstream sections of the catchment using the expected annual damage (EAD) as indicator. By looking into this effect for different protection configurations upstream, new knowledge will be gained on the correlation between embankments and flood dynamics at the catchment level.

1.1.3. Research Questions

To reflect the ambition stated in the research objective, a central research question is raised:

> How does the effect of river embankments on flood propagation change the risk of flood in a catchment?

This is addressed through the sub-questions:

a. How does the configuration of flood protections upstream change the flood hazard downstream?
b. How does the avoided EAD compare to the inflicted EAD in the catchment, as result of the configuration of flood protections in the catchment?

1.2. Theoretical research approach

The concepts outlined in the research objective necessitate to be placed in a relevant theoretical context. For this reason, the consolidated framework used in river flood risk studies and management practice is described using the most recognized definitions in the field.

1.2.1. River flood risk framework

Risk is defined by the United Nations Office for Disaster Risk Reduction (UNDRR) through the Sendai Framework as the combined effect of three elements (UNDRR, 2015): hazard (the frequency and associated intensity of a natural event), exposure (the lives and assets potentially in contact with the hazard) and vulnerability (the harm occurring to the exposed lives and assets in case of occurrence. These concepts have been inflected to represent the specific risk of flood and consolidated through the exhaustive work of several authors (Meyer et al., 2013). Hazard is the dimension of risk that is most pertinent to the hydrological event of flood, being represented by the probability of exceedance p associated with the occurrence of flows of a certain magnitude. Extreme values curves illustrate this relationship through a plot of the distribution of maximum flows recorded in a period over their frequency of occurrence. The first step in fluvial flood risk analysis is to retrieve such curve for the river reach and apply a statistical analysis to extrapolate a standard series of maxima. For each of these events (and associated probability), a spatial distribution of flood depth can be constructed. Exposure depends on the socio-economic value of the inundated area, providing the base for the impact assessment. It is normally described using a spatially distributed economic indicator, such as the gross domestic product, or a land use/cover map (Winsemius et al., 2013). Finally, vulnerability can be interpreted at different levels of complexity, accounting for direct damages only or including indirect-, business interruption- and intangible-damages (Meyer et al., 2013). In general, this is included in a vulnerability function, which relates the flood depth to the expected damage D on the basis of an empirical or synthetic relationship, specific for the land-use type and study area (Merz et al., 2010).

Risk is quantified through an exceedance probability-loss (EPL) curve where each i-th point describes the impact EPL_i of an event associated to a specific probability of exceedance p_i (De Moel et al., 2014; Meyer et al., 2009). The EAD is given by the area subtended by the continuous impact-probability function, i.e. the integral described by the equation:

$$EAD = \int_{p_0}^{p_1} EPL(p)dp \qquad [2.1]$$

The effect caused by presence of the embankments on the catchment will be reflected by the changes in the outcome of the risk function. Using the hypothesis that embankments change the risk of flood downstream, this correlation will be revealed by an increase of the damage for a certain return period event. Considering the magnitude-frequency relationship which floods abide by (Wolman & Miller, 1960), this is equivalent to say that events associated to a certain damage will occur more frequently. These changes will occur independently of the exposure or vulnerability, signifying that hazard is the level at which embankments and risk interact.

1.2.2. Protection standards and risk

To overcome the limit reached by previous studies in addressing the issue of downstream flood aggravation, river embankments have to be fit in the architecture of risk. This starts by considering the occurrence of overbank flow that follows when the stage of the river is higher than the crest of the embankment. The probability that this level is exceeded by the river can be put in terms of the return period, or average recurrence time of the same event, defined with:

$$T(X) = \frac{N}{r} \qquad [2.2]$$

Where X is the river stage or discharge in the event, N the number of years during which the event occurs r times (Shaw et al., 2010). Hence, an embankment of a certain height ensures a specific flood protection level, it being the return period of the flood needed to overtop it. Flood damage has been demonstrated to have a high sensitivity to the protection standard in place (Ward et al., 2013). Moreover, since it includes region-dependent variables of the hydrological regime and specific dike height, it allows for a proportionate cross-region comparison. Additionally, protection standards can be considered uniform on large scales; this facilitates data collection, e.g. to create a global database (Scussolini et al., 2016), and policy relevant data sharing, since a country or region can be described in terms of the flood protection level in place and the potential annual damage arising from it (see the Aqueduct Global Flood Analyzer initiative: www.wri.org/floods and in Ward et al., 2020).

1.3. Contribution of the research

The contribution of this study to the previous and on-going research efforts consists of creating an original conceptual model of the flood defence and flood risk relationship. Bringing information to enhance

this understanding could question the approach adopted by risk evaluation models. These often assume uniform protection standards over large areas and consider only the 'positive' effect of applying this measure for risk reduction, without questioning how their hydrological interaction could result in a more complex spatial risk distribution. This is a significant approximation that could be reconsidered to achieve a more accurate risk assessment. The importance of advancing our model representativeness has been well substantiated in Ward et al. (2015), where it is affirmed that the research agenda of global hazard and risk models calls for "an improved representation of fundamental physical and socioeconomic processes leading to flood impacts". With this research, it will be clearer whether the effect under investigation has a dimension that justifies the effort of flood modellers to include in their analysis.

2. Materials and methods

This chapter aims to provide a thorough overview of the technical design of the research. First, the study area is described, after which follows an outline of the general structure and objective of the methodology and of the scenarios setup. Next, the modelling framework and parametrization is detailed, followed by the analysis performed with the model and on the model outcomes.

2.1. Study area

The study is conducted on the section of the Rhine river that goes from the 'Niederrhein', at the German city of Köln, to the terminal and delta section of the river (Figure 3). The construction of high dikes in the German section of the Rhine has been a matter of controversy[1] and has been discussed in programs on the trans-boundary catchment development (ICPR, n.d.).

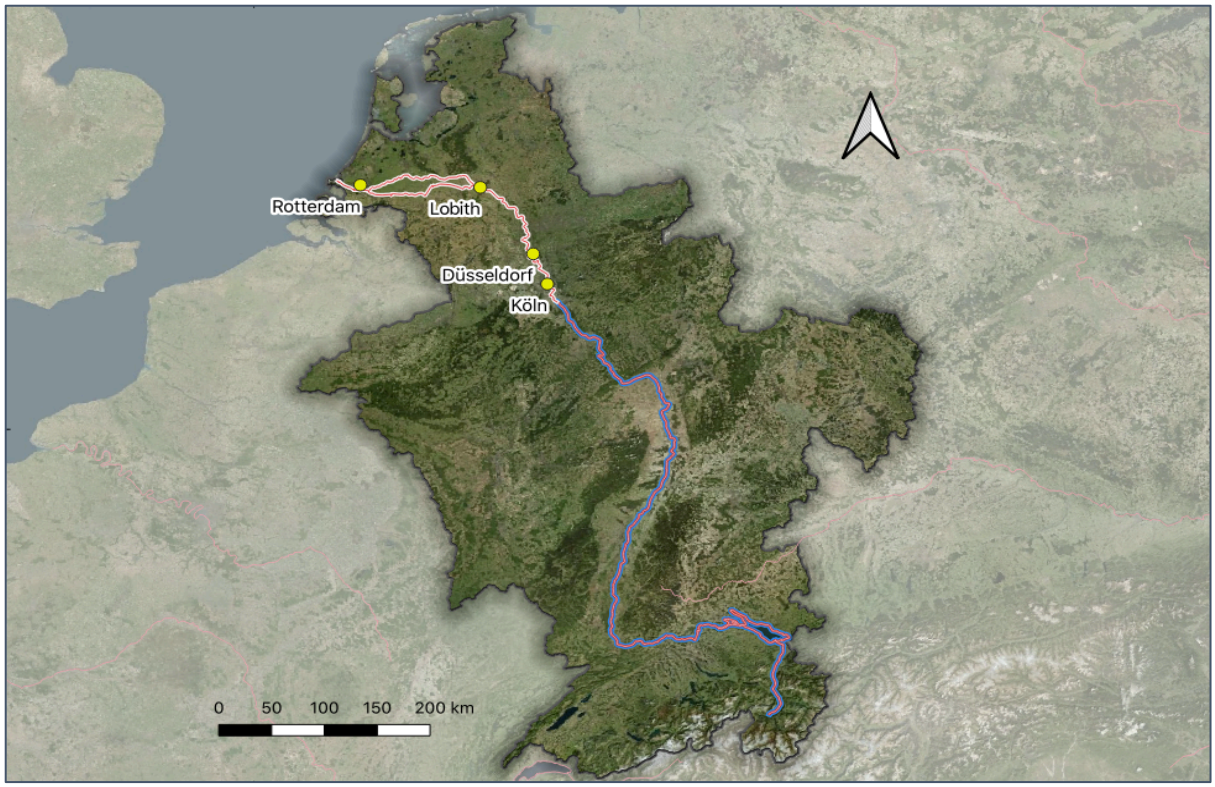

Figure 3: comprehensive representation of the entire Rhine catchment. The section of interest, approximately from the city of Köln to the delta, is represented in red and white (Projection: EPSG 32361).

The river catchment of the Rhine is delineated from the Digital Elevation Map (DEM) described in §2.4. using the deterministic drainage network extraction algorithm from O'Callaghan & Mark (1984), which is based on a steepest elevation gradient analysis to determine the flow direction and to provide a drainage network. By specifying the drainage outlet position, all the cells that provide a flow contribution to that

[1] https://english.deltacommissaris.nl/delta-programme/question-and-answer/what-about-the-18000-m3-river-discharge

point are extracted, and the catchment is delineated (Figure 4). The downstream part of the Rhine and the Meuse catchments are characterised by the absence of significant elevation gradients, which invalidates any attempt of catchment delineation by gravity. Here, we refer to the river catchment database of the European Environment Agency (EEA). The Meuse and its catchment are included in the model domain since the river merges with the Rhine in the delta and interacts with its hydrologic behaviour. Excluding the Meuse river from the model could introduce significant errors in the simulations, as the river drains the southern part of the floodplain. On the contrary, the Ijssel river is left out of the model domain as it is not directly contributing to the flood risk in the catchment; this will introduce a variable error in the results, as the flow in the channel depends on that of the main reach and contributes draining the floodplain; this aspect is discussed further in the validation (§ 3.1.2.).

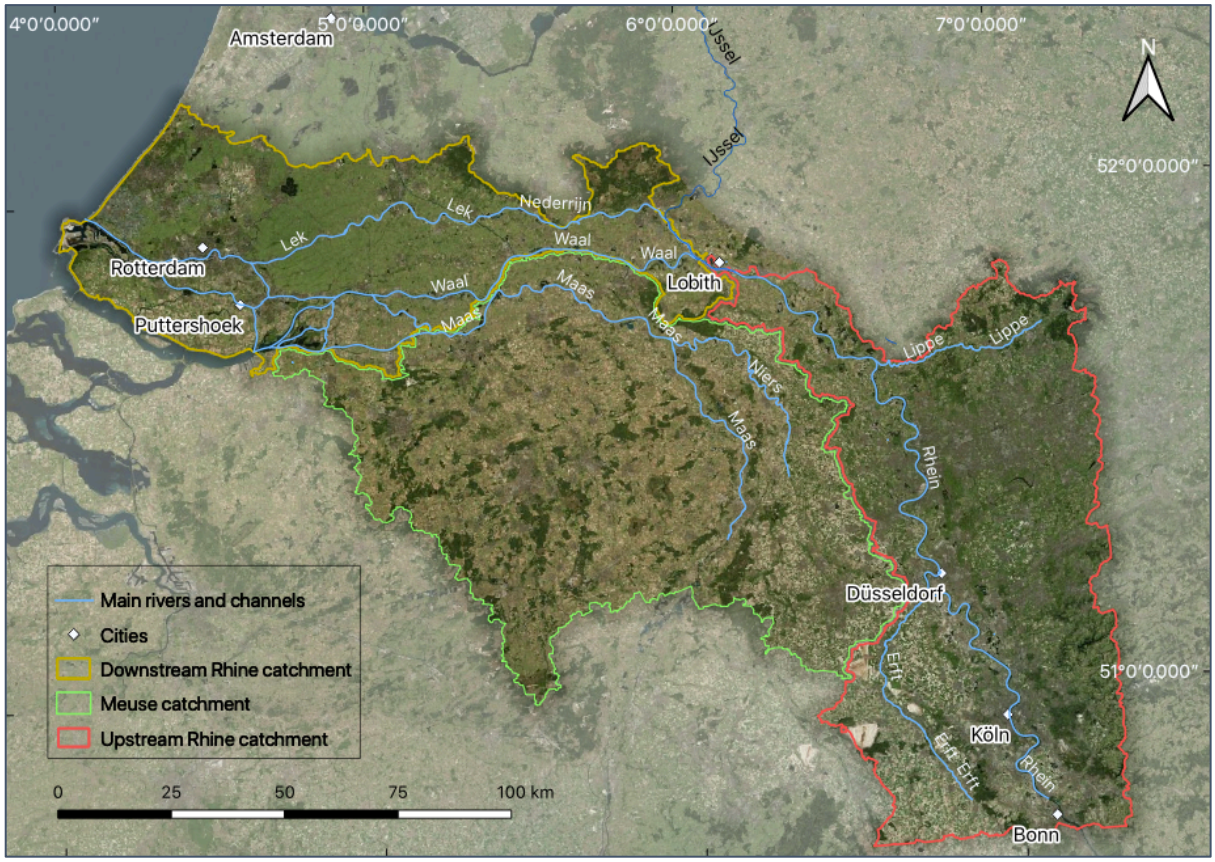

Figure 4: The main rivers, cities and boundaries of the three catchments found from the deterministic catchment delineation algorithm (Upper Rhine Catchment) and from the EEA database (Lower Rhine and Meuse Catchment, projection: EPSG 32361).

In order to facilitate the discussion on the hazard and risk propagation in the catchment, the study area will be sub-divided into the German (Düsseldorf and Cologne) and Dutch (Gelderland, Noord-Brabant, Utrecht, Zuid-Holland) administrative regions of the domain[2] (Figure 15 in the results, § 4.1.3.).

[2] Areas modified from the Database of Global Administrative Areas (Hijmans et al., 2010). Available at: http://globe.umbc.edu/documentation-overview/global-administrative-areas-gadm/

2.2. Outline of the procedure

The experimental procedure consists of a parametric analysis of flood hazard and risk based on the upstream flood protection configuration as independent variable. Previous studies provide a general way forward for flood risk modelling which involves a modular approach that combines an inundation hazard-with a flood impact-module (Arnell & Gosling, 2016; Ward et al., 2013, 2017; Winsemius et al., 2016). Such approach is reproduced here, allowing to break down the analysis of risk and evaluate the parameters defining hazard and risk separately, providing distinct answers to sub-questions a and b.

The hydrological-hydrodynamic coupled modelling framework of GLOFRIM (Hoch, Neal, et al., (2017); further described in § 2.3.) is used to assess flood hazard and to feed a damage assessment model. The flood hazard assessment and the damage assessment carried out for the study are respectively referred to as STEP 1 and STEP 2 of the research (Figure 5). The objective of these steps is retrieving a series of variables dependent on the protection configuration and indicative of hazard and risk in the catchment (green boxes in Figure 5). In particular, information will be generated on the extreme flow values, hydrograph propagation and inundation maps in the catchment for hazard, and the EPL curve values for risk.

The analysis starts with STEP 1 (blue box in Figure 5) by simulating a Base scenario, where both the downstream and upstream sections of the catchment are non-protected. This provides the baseline condition for the catchment, from which the 10, 50, 250, 500 and 1000 years return period flows are extracted using a Gumbel extremes distribution analysis (Gumbel, 1941). Based on these flows, 5 protection scenarios are designed for the upstream section (Table 1). For each scenario Method A and Method B are used to provide the hazard variables separately. Method A (detailed description in § 2.5.1) is based on the approach of Ward et al. (2013). It applies a statistical analysis on the daily inundation time series to obtain a specific return-period inundation depth value. Method B (detailed description in § 2.5.2) simulates the hydraulic inundation events for the same return periods using a synthetic hydrograph. STEP 2 uses the flood maps delineated with these two methods to generate an EPL curve, based on a damage calculation routine (detailed description in § 2.6.). Since two independent series of maps are generated in the previous step (for Method A and B), two comparable risk results are obtained.

Table 1: Scenarios considered for the simulations.

Upstream river configuration						
Protection Standard (years)	Non-protected	10	50	250	500	1000
Scenario	Base	Prot10	Prot25	Prot250	Prot500	Prot1000

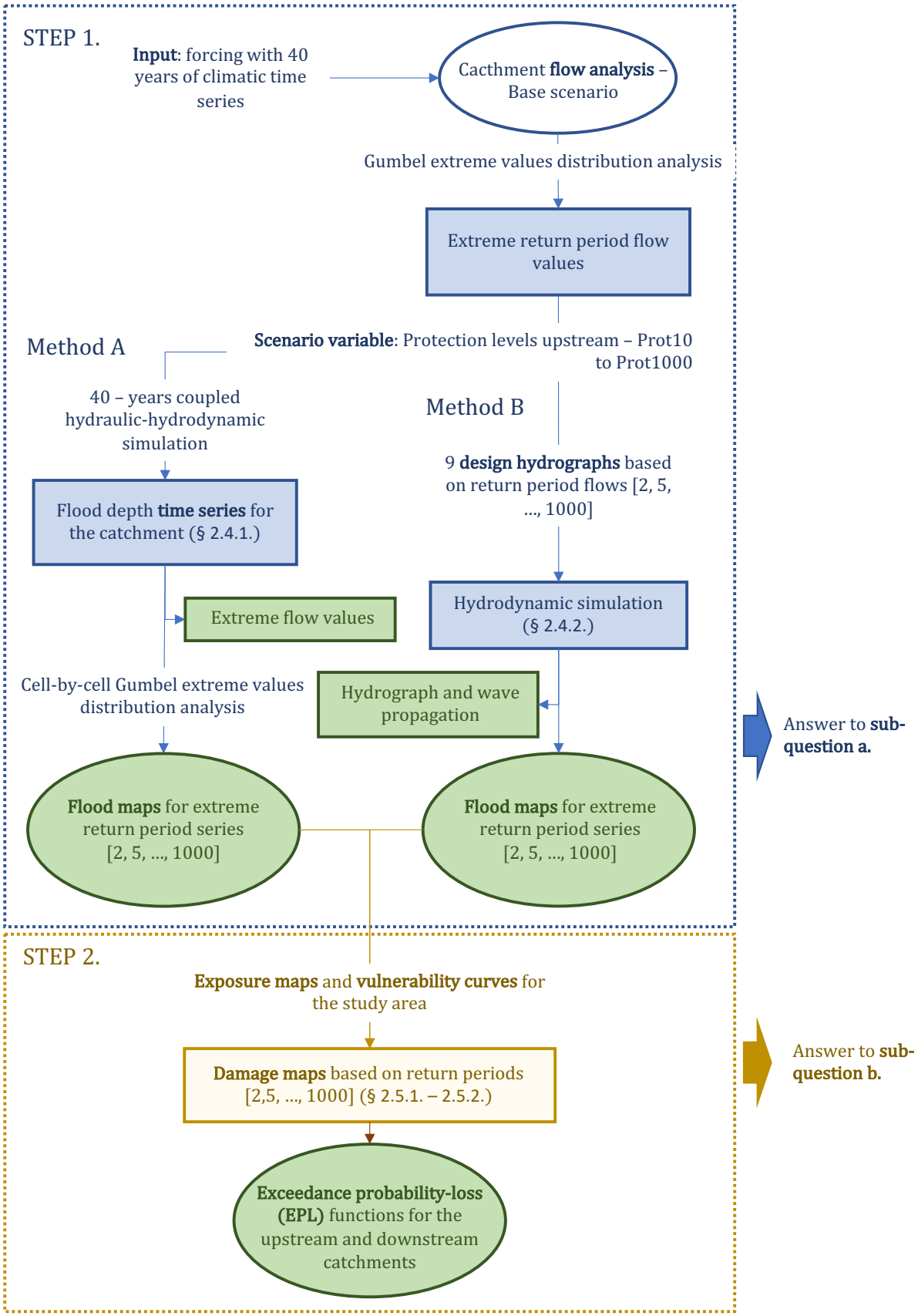

Figure 5: Flow diagram of the research methodology.

2.3. The GLOFRIM modelling framework

Two conditions have to be accounted for while choosing an appropriate inundation modelling scheme. First, the goal of retrieving a representative time-series of the target values (discharge and inundation depth) for the study area and period. For this objective to be achieved, a hydrological model needs to be forced with a time-series of climatic and human water use data. On the other hand, the investigation of the physical phenomenon requires, in terms of both hydraulic model complexity and spatial resolution, a more sophisticated representation than the one allowed by large-scale hydrological models. Several of these have experienced in recent years significant improvements towards inter-model agreement, providing uniform inundation results for large regions (Trigg et al., 2016); however, they lack detailed resolution and hydrodynamic representativeness. The issue of combining these two facets has led to the development of a Globally applicable computational FRamework for Integrated hydrologic-hydrodynamic Modelling (Hoch, Neal, et al., 2017), hereafter GLOFRIM[3]. The one most noticeable feature of this tool is that it allows to achieve the on-line (on a time-step basis) and spatial (on a grid-cell basis) coupling of two models of choice where hydrological variables are recursively updated and fed as input forcing to the hydrodynamic solver during the simulation. While several improvements have included new model extensions and coupling schemes (Hoch et al., 2019; Hoch, Ikeuchi, et al., 2018) and extension to the groundwater domain (Eilander et al., 2018) leading to a second version of GLOFRIM, the most basic setup is congenial here to reach the study objective. In this configuration, the hydrodynamic model is nested in the hydrological model in the bounds of the study area only, whereas the hydrological model runs in stand-alone mode in the larger Rhine-Meuse catchment, employing a simplified scheme to route water (Figure 6). This allows to achieve the contemplated level of detail in the study area while avoiding rough oversimplifications and including the hydrological contribute from the entire catchment at a reasonable computational cost.

2.3.1. Model hydrology

The physically-based hydrological model PCRaster Global Water Balance[4] (hence forward PCR-GLOBWB), first developed by van Beek & Bierkens (2009) and its GLOFRIM implementation have been extensively employed to benchmark different hydrodynamic models (Hoch, Neal, et al., 2017) and modelling configurations (Hoch et al., 2019; Hoch, van Beek, et al., 2018). Moreover, the value of PCR-GLOBWB in large-scale flood risk studies was endorsed by its successful application at the global scale to power the hazard module of GLOFRIS (Ward et al., 2013; Winsemius et al., 2013; further described in § 2.6.). The model algorithm solves the water balance on a grid cell basis by considering a set of fluxes at each time step. In the most recent version (Sutanudjaja et al., 2018), water within a cell is exchanged through vertical fluxes between soil and groundwater storage volumes, between the land surface and the atmosphere through precipitation and evaporation fluxes and horizontally between the land surface- and groundwater-storage and surface water by accounting for baseflow, interflow and runoff. In addition,

[3] Online documentation at: https://glofrim.readthedocs.io/en/latest/index.html
[4] For latest updates see: https://globalhydrology.sites.uu.nl/research/models/

distributed data on industrial, domestic and agricultural demand accounts for the net water abstraction from the hydrological cycle, allowing to include the anthropogenic influence and hence increasing the model representativeness of historical time series. Water is exchanged between different cells by mean of surface water routines based on maps of local drainage cell directions (van Beek & Bierkens, 2009), providing a measure of discharge that allows to benchmark the model with gauged river flows.

The resolution at which the model operates has a significant influence on the overall discharge simulation accuracy since of the two available versions, at 30 and 5 arcminutes, the latter is capable of reproducing fine-scale processes with whom the former struggles, such as snowmelt (Sutanudjaja et al., 2018). However, the model's performance will also be affected by the routing method, which can be chosen between a simple water accumulation- or characteristic travel time-based scheme and the kinematic wave form of the shallow water equations. When PCR-GLOBWB is employed in GLOFRIM, these considerations are relevant outside of the coupled domain, where PCR-GLOBWB runs in stand-alone mode. Nevertheless, when the centroid of (at least) one hydrodynamic model cell lies in the bounds of a PCR-GLOBWB cell, the surface water routing scheme of PCR-GLOBWB is taken over by the hydrodynamic model solver. In this case, the accuracy in simulating discharge and inundation extent is univocally dependent on the hydrodynamic model configuration (Hoch, Haag, et al., 2017), which becomes performance-determining.

2.3.2. Model hydrodynamics

The hydrodynamic model Lisflood FP[5] (Bates & De Roo, 2000) has been adapted to GLOFRIM compatibility and benchmarked for this purpose in a large-scale flood modelling case study, demonstrating good results and runtime performance (Hoch, Neal, et al., 2017). The model solves the continuity and momentum equations at each time step through an explicit difference scheme. After the first formulation, progressive improvements in stability (Hunter et al., 2005) and to include more sophisticated solvers (Bates et al., 2010; Neal, Schumann, et al., 2012; Neal, Villanueva, et al., 2012) have been achieved. This has provided the user with an increasingly varied choice of governing equations, model complexity and dimensional setup to describe water propagation in the floodplain and channel. In this study, the extent of the spatial domain requires a grid resolution (further discussed in §2.4.) significantly larger than the medium to high resolution which Lisflood was originally designed for (25-100 m). For applications of this type, the large cell size could misrepresent floodplain connectivity leading to significant modelling errors, an issue exacerbated by the flat topography of the study area. To overcome it, the sub-grid channel formulation developed by Neal, Schumann, et al. (2012), which allows to specify the river width at a different resolution than that of the grid cell, is used. In this setup, water is routed in the channel through a 1D scheme, while floodplain routing (which occurs when the channel flow capacity is exceeded) follows a 1D scheme over a 2D grid, where the solving equation is coupled in both directions. At each time-step, a discrete form of the continuity equation:

[5] For latest updates see: http://www.bristol.ac.uk/geography/research/hydrology/models/lisflood/

$$\frac{\Delta h}{\Delta t} = \frac{\Delta Q}{\Delta x \Delta y} \qquad [3.1]$$

and the momentum equation (here one-directional) with the convective acceleration term neglected (Bates et al., 2010):

$$\frac{\partial q}{\partial t} + \frac{gh\partial(h+z)}{\partial x} + \frac{gn^2q^2}{R^{4/3}h} = 0 \qquad [3.2]$$

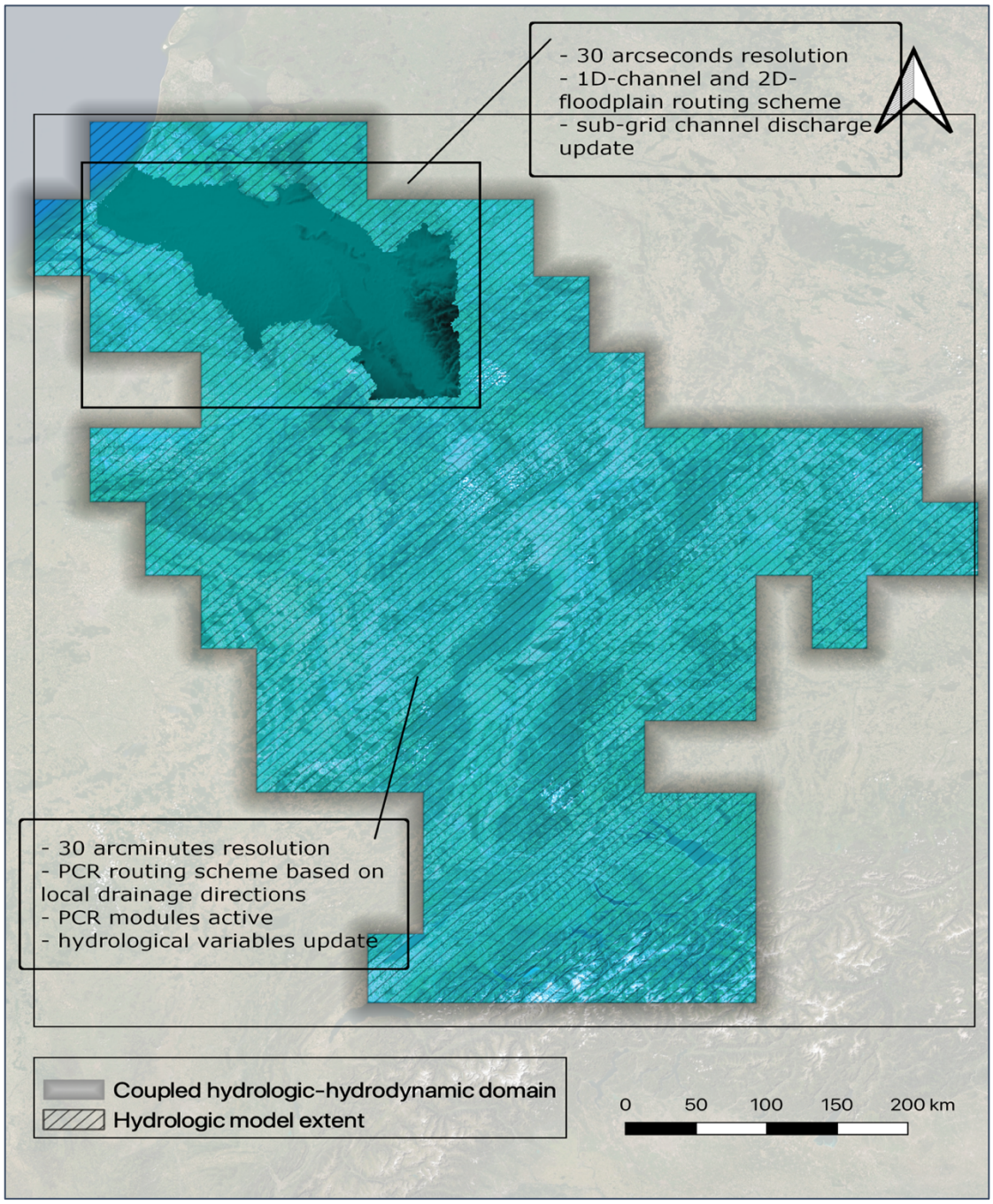

Figure 6: Schematization of the overall model domain to represent the nested setup.

are used to update the water balance for each cell, where $h[m]$ is the surface height, $x, y[m]$ are the cell dimensions, $g[ms^{-2}]$ is the gravity constant, $R[m]$ is the hydraulic radius, n $[-]$ is Manning's friction, $t[s]$ is time and $Q[m^3s^{-1}]$ and $q[m^2s^{-1}]$ are the volumetric and unidimensional-width flow, respectively. This inertial formulation of the momentum eq. is used to compute both the 1D-channel and the 1D/2D-floodplain flow, with the difference that additional terms for the bed elevation and width are included in the channel solver. This setup has been tested and applied in large-scale modelling studies (Neal, Schumann, et al., 2012; Sampson et al., 2015), demonstrating that under this condition the sub-grid channel allows to capture hydraulic and inundation characteristics more accurately than previous formulations.

2.4. Parametrization of the hydrodynamic domain

To represent the spatial domain of the model, the 'Bare-Earth' product is used as starting point, consisting of a vegetation-corrected Shuttle Radar Topography Mission (SRTM) DEM at 3 arc-seconds resolution (O'Loughlin et al., 2016). On top of being generally more accurate than the SRTM, this product resolves better the floodplain connectivity, which is beneficial to represent the flood distribution in the study area. The 'Bare-Earth' product may contain imperfections such as local topography depressions which act as sinks, accumulating water and introducing artefacts in the simulations. For this reason, the surface depression-removal algorithm of Wang & Liu (2006) is used to eliminate these sources of noise. Next, the resolution of the grid is re-scaled to obtain the final 2D cell size input for the model (Figure 7).

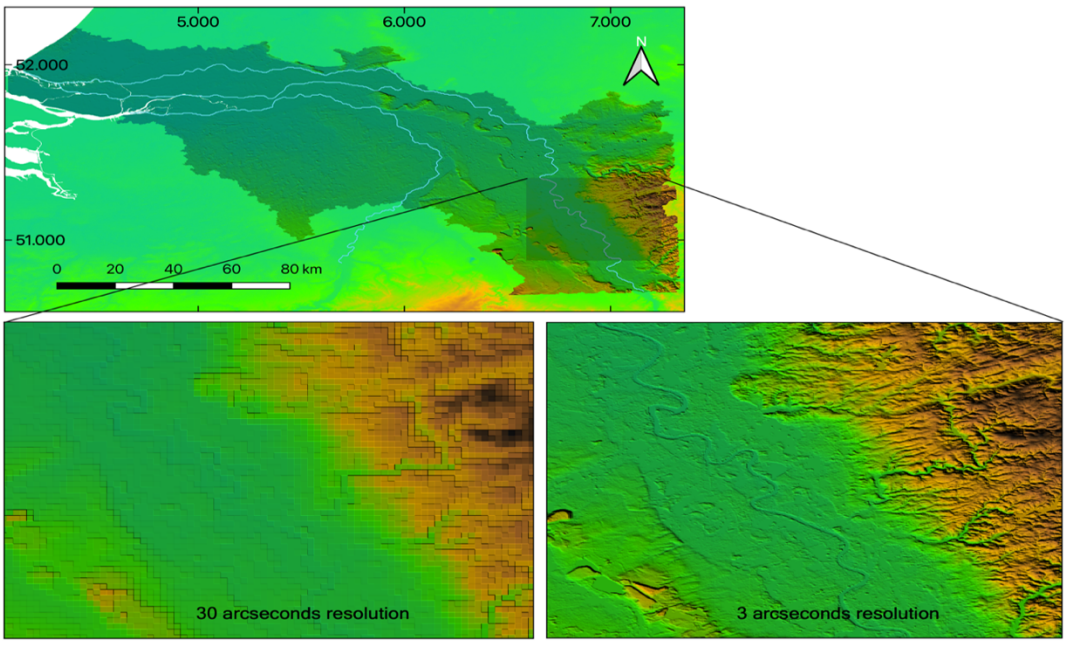

Figure 7: 30 arc-seconds (bottom-left) and 3 arc-second (bottom-right) DEM at comparison (projection: EPSG 4326).

The high resolution of the 'Bare-Earth' product exceeds the computational effort allowed to respect reasonable time constraints and overcomplicates the modelling process. Moreover, upscaling the grid resolution allows to reduce the vertical errors of the DEM by averaging the cell values. In agreement with Neal et al. (2012), a normal error distribution reduces by a factor of $1/\sqrt{N}$, where N is the number of resampled cells, meaning that N=100 will reduce the error to 0.1 of the original value. Considering that the 'Bare-Earth' has generally a lower error than the original SRTM DEM, the floodplain connectivity is represented with a confidence of at least 95% (Neal, Schumann, et al., 2012). This is particularly important considering the flat topography of the study area in the downstream region. Therefore, the DEM was resampled to a resolution of 30 arc-seconds, which corresponds to roughly 600 x 900 m at the latitude of the study area.

2.4.1. Sub-grid channel characteristics

The user-defined information on river location and geometry required by the sub-grid channel setup is retrieved from the MERIT hydro[6]: global hydrography dataset (Yamazaki et al., 2019), which includes global raster format maps of river width at 3 arc-seconds resolution. The river width map is resampled at the resolution of 30 arc-seconds to match the two grids, using a nearest neighbour method allowing to preserve the original values at the upscale resolution. To determine the channel geometry, the channel depth needs to be specified along with the river width. However, such information is in general more difficult to retrieve since bathymetric measurements are not available over large regions. To overcome this issue, the channel hydraulic geometry theory described by Leopold & Maddock (1953) is invoked, describing the relation between discharge below bankfull and the channel geometry parameters through a set of power law expressions of the type:

$$d = m * w^k \qquad [3.3]$$

where d (m) is the channel depth, w (m) is the channel width and m, k are calibrated coefficients. Andreadis et al. (2013) produced a global dataset of river bankfull width and depth based on this theory, which considers the 2-years return period flow as the bankfull capacity of the channel. The information included in the database[7] are plotted to extrapolate a graph of depth v width for the river Rhine. After fitting the power-law relationship (with $R^2 \sim 1$ for the fitting), it is found that $m = 0.058$ and $k = 0.78$. Using this parametrization of equation 3.3 and the channel width from the MERIT hydro database, the riverbed elevation can be found. This defines the geometry of the rectangular sub-grid channel network that is overlaid on the 2D floodplain model (Figure 8). A fixed water surface elevation of 0 m is applied as boundary condition at the edge of the channel network. In agreement to previous measurements of the channel bed roughness (Julien et al., 2002), Manning's n is uniformly set to the value of 0.03 [-] whereas the floodplain roughness is set to a unitary value of 0.05 [-], which is in the suggested range, considering the overall low sensitivity to this parameter (Werner et al., 2005).

[6] Available at: http://hydro.iis.u-tokyo.ac.jp/~yamadai/MERIT_Hydro/

[7] Available at: http://gaia.geosci.unc.edu/rivers/

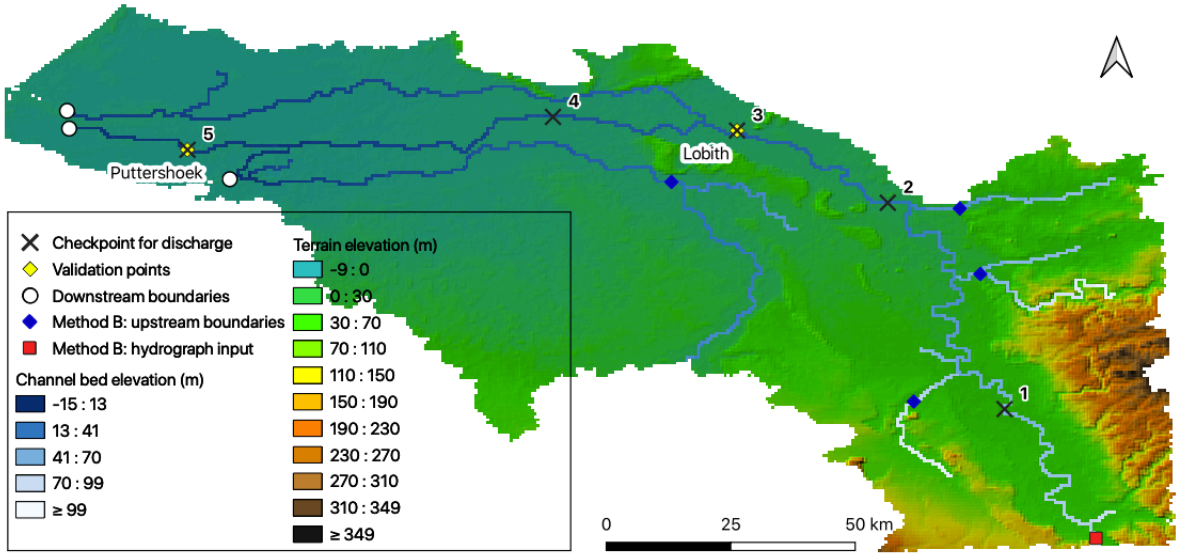

Figure 8: Floodplain 2D model grid (DEM) and sub-grid channel network specifying the bed elevation of the 1D model projection: EPSG 4326).

2.4.2. Representation of river embankments

The issue of incorporating flood defences in hydrodynamic simulations has daunted flood modellers since computational advances have allowed for large-scale representations of inundation dynamics. This is because the typical dimension of features such as river embankments is not grasped by the resolution of global topography datasets (Wing et al., 2019) and cannot be implemented at the working resolution of large-scale models, leading to an overall flattening and underestimation with regard to their topological signature.

In previous works, this issue has been dealt with by employing a sufficiently fine resolution along with local defence information datasets (Wing et al., 2017), by accounting for the protection offered by defence structures as a post-process step (Ward et al., 2013) or, in recent times, using a feature-detecting algorithm trained on ground-truth data to recognise flood defences over large regions and upscale them to coarser resolutions (Wing et al., 2019). These methods however cannot cope with the 30-arc sec resolution applied here along with the need to represent flood defences as a process step, and not in hindsight. These reasons lead to the choice of 'burning' the embankments into the DEM by specifying the crest elevation for the cells corresponding to the river channel. As the sub-grid channel bed elevation is defined separately and kept constant, this will increase the total conveyance and simulate the physical effect of embankments. As pointed out by Wing et al. (2019), the unintended consequence of this representation is that it will interact with the terrain profile and will have an effect on the flood distribution in the immediate proximity of the channel, by increasing the elevation gradient between the raised cells and the ones in their proximity. For this reason, the floodplain flow could have a higher inertia and propagate further, when overbank flow occurs. However, Lisflood does not compute lateral flows directly between the channel and the floodplain (Neal, Schumann, et al., 2012), therefore the new configuration should not have an effect

on return flows to the channel. Based on the methodology described in § 2.2. and by using the extreme discharges measured at Lobith in the Base scenario, the configurations for scenarios Prot10 to Prot1000 are delineated (Figure 9). Considering that the sub-grid channel cross section is rectangular, Manning's equation applies to calculate the desired channel depth from the return-period discharge, using the approximation of the hydraulic radius for large and shallow river channels:

$$Q = \frac{1.486}{n}\sqrt{S}\, L \sqrt[3]{h^5} \qquad [3.4]$$

Where $R\,(m)$ is the hydraulic radius, $S\,(-)$ is the channel slope in the embanked section, $L\,(m)$ is the river width, $A\,(m^2)$ is the channel cross-sectional area, n is Manning's coefficient and $h\,(m)$ is the desired channel depth.

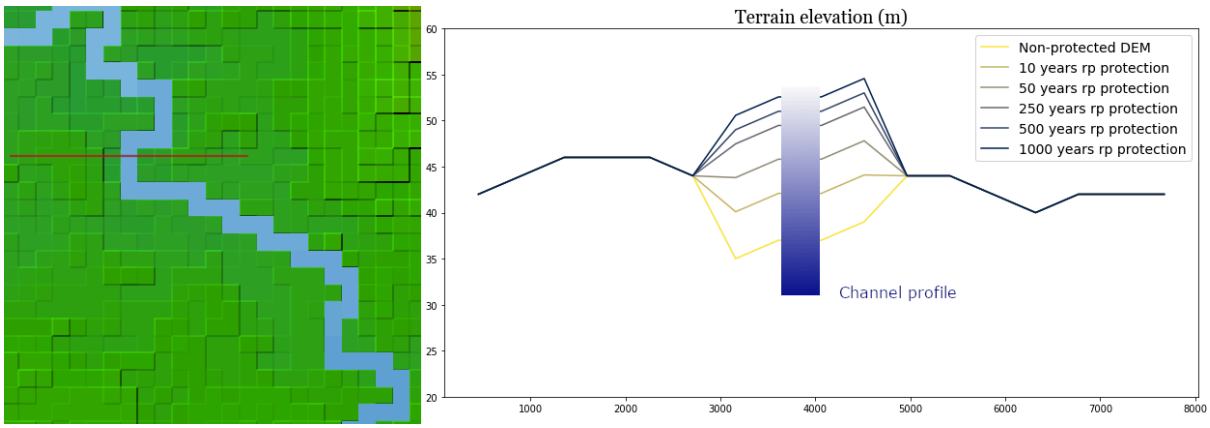

Figure 9: Channel profile and elevation profile of the embankments along a transect of the study area (image on the left). On the right, different protection level profiles are shown. Notice that the channel appears narrow because of the scale used in the image.

2.5. Step 1: Inundation hazard

2.5.1. Method A: statistical approach

This method is a modified version of the approach used in (Ward et al., 2013) for the inundation modelling. Using GLOFRIM, a 40-year long time series of flood depth values is retrieved in each cell of the study area, for the period 1960-2000 (details of the run in § 3.1.). To obtain the inundation maps corresponding to 2, 5, 10, 25, 50, 100, 250, 500 and 1000 years of return period, the annual maxima are extracted from the time series. The series was set to start in September and end in August, in order to obtain the values corresponding to hydrological years. The statistical treatment of extreme values from this collection of data falls under the extreme value theory. A generalised extreme value distribution such as the Gumbel distribution (Gumbel, 1941) can be applied to estimate the magnitude associated to a

certain frequency of recurrence from the series of maximum values. It consists of a statistical analysis of reciprocally independent maximum values taken at defined time intervals in a temporal distribution and is often applied in hydrology to time series of flow. The method of moments (Shaw et al., 2010) allows to obtain the parameters a and b of the Gumbel (EV1) equation:

$$F(X) = \exp\left[-e^{-\frac{X-a}{b}}\right], \quad for: \; F(X) = \frac{T(X)-1}{T(X)} \qquad [3.5]$$

where $F(X)$ is the probability that the annual maximum X is not exceeded and $T(X)$ is the related recurrence interval. By recombining this equation for flood depth D (m), the following expression can be obtained:

$$\widehat{D_r} = a - b * ln\left[ln\left(\frac{T_r}{T_r - 1}\right)\right] \qquad [3.6]$$

where $\widehat{D_r}$ is the return-period water depth. Using the values found for a, b this expression can be used to extrapolate the specific return period-depth (2, 5, …, 1000) from the recurrence time associated to it. Since the hydrological year is taken as basis for the annual maxima series, the assumption of statistical independency of the values is not violated. By aggregating all the equal return period depths, the inundation distributions are found. The 2-year return period flood is considered not to lead to flooding as the bankfull discharge has the same return period. Therefore, the hazard map corresponding to this value is subtracted from all others to avoid overestimations. This procedure is applied on Method B, too.

2.5.2. Method B: hydrodynamic event-modelling approach

This method is based on the hydraulic simulation of each return period-event in the series 2, 5, 10, 25, 50, 100, 250, 500, 1000 years. The approach requires a design hydrograph to represent the flow occurring with these return periods. This is then routed in the channel and study area using the capacity of the hydrodynamic model Lisflood in stand-alone mode. The hydrograph-defining method used here is based on a combination of the Soil Conservation Service (SCS) synthetic hydrograph method (NRCS, 2007) and an efficiently simplified version of the procedure detailed in Kramer (2012). The steps and choices required to derive the design hydrographs are further substantiated in Appendix A. The discharge time series of which the empirical hydrograph delineation is based off is obtained once again from the Base 40-year simulation using GLOFRIM (details of the run in § 3.1.1); this is to maintain consistency between the design floods and the protection levels assumed in the model. The procedure of hydrograph delineation is applied to the discharge time series in Bonn as the most upstream point of the hydrodynamic domain (§ 2.4.). Hence, the hydrographs retrieved for each return period are used as inputs in the scenarios Base to Prot1000. This yields a total of 54 hydrodynamic simulations for cross-scenario comparison. For Method B, every simulation lasts for roughly 20 days, on the basis of the time to peak calculated for the Rhine catchment at the inlet point of the hydrodynamic domain, and the observed time taken for the flood wave to travel to the end of the domain.

The absence of a hydrodynamic model that backs up the simulation by exchanging its variables, as happens in GLOFRIM, requires a deeper intervention of the modeller on the simulation set-up, since upstream boundary conditions need to be imposed in the hydrodynamic domain corresponding to those tributaries that would otherwise be coupled to a PCR-GLOBWB cell. In this case, the boundary conditions outside the main channel are set up by using the average 1D channel flows measured during the 40-year GLOFRIM simulation. Although this could misrepresent important characteristics of the overall hydrodynamic behaviour of the domain (such as the effect of combining flood peaks, traceable in the discussion § 4.1.3.), it reduces the variables that have an impact on the system and sets up the condition for a parametric study (Straatsma & Huthoff, 2011).

2.6. Step 2. Inundation risk through impact modelling

Step 2 regards the procedure used to obtain a value of flood risk for the catchment from the two series of hazard maps of Method A and B. The two general stages of this procedure are the calculation of the damage associated to a flood depth map and the estimation of the EPL curve from the damage at each return period (2, 5, …, 1000 years). For the hazard dataset obtained through Method A, the damage calculation is applied directly on each return-period flood depth distribution map. Method B yields for the return period-hydrographs a series of maps that describe the progress of the flood wave through the floodplain in the timespan of the event. Therefore, the maximum inundation extent for each event is chosen to portrait the largest value of potential damage.

2.6.1. Damage assessment

The total direct damage for a hazard map is calculated following the methodology of Tiggeloven et al. (2020).The flood depth values are combined with distributed data on exposure; for this study, this is represented by the maximum economic value of the built-up area, sub-divided in residential, commercial and industrial occupancy type. The relative abundance of each category is assumed to be constant and corresponding to 75% residential, 15% commercial and 10 % industrial based on remote sensed and census-based data (Economidou et al., 2011; Soukup et al., 2016). For each cell, a percentage value representing the relative occupied surface is assigned by matching the 30 arcsecond-resolution 2UP dataset (Van Huijstee et al., 2018) to the grid of the inundation maps, using a nearest neighbour resampling algorithm (Figure 10). This value is then multiplied with the total cell surface to obtain the occupied surface in squared kilometres. Following Huizinga et al. (2017), a maximum economic value $V_{m,o}$ expressed in Purchase Power Parity (PPP) per surface can be assigned to the three occupancy types (residential, commercial or industrial), based on the country. This allows to obtain a normalised economic value per cell that can be used for cross-country comparison, as PPP levels the difference between the national economies present in the research area. To reflect the different vulnerability of the inundated assets, three depth-damage functions are considered based on the estimates of Huizinga et al. (2017), representing each occupancy type. These functions (Appendix B) express damage as a percentage of the total asset value,

according to the water level. By recalling the theory of flood risk, the damage associated to the flood level in a cell is retrieved through:

$$D_o = V_{m,o} * v_o \qquad [3.7]$$

where D_O $[PPP/km^2]$ is the damage associated to each occupancy type and v_o [%] is the percentage value obtained from the vulnerability-depth functions for the specific water depth found in the cell, indicating the damage inflicted by the flood as a fraction of the maximum asset value. The procedure yields a distributed damage value associated to a specific return period.

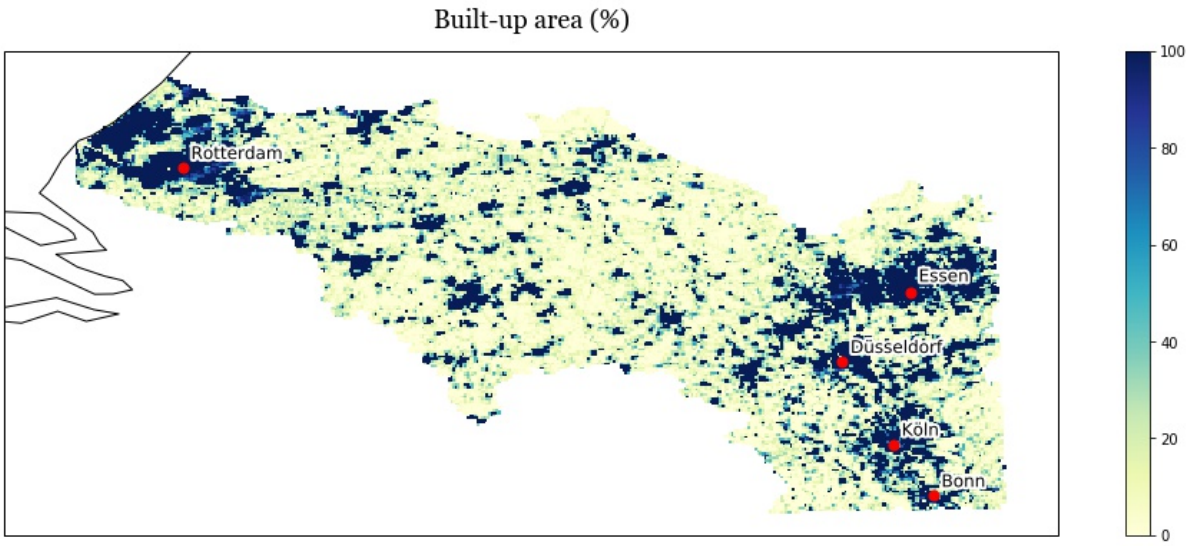

Figure 10: Exposure map for the study area obtained by resampling the 2UP dataset (Van Huijstee et al., 2018). The urban areas of Rotterdam and den Haag in top-left of the frame, as well as Bonn, Düsseldorf and the Ruhr area in the bottom-right corner are clearly visible in dark blue.

2.6.2. Calculation of flood risk

A unique return period-damage is obtained by simply aggregating the damage found for all cells in the domain. This damage is then associated to a probability of exceedance knowing that:

$$P(X) = 1 - F(X) \qquad [3.8]$$

where the probability of non-exceedance $F(X)$ is related to the return period by eq. 3.5. With this, an EPL curve is constructed for probabilities corresponding to the range 2 to 1000 years of return period and extrapolated to 10000 years. This is because beyond this point do not affect the risk outcome significantly (Ward et al., 2011). The integral under this curve is computed using a trapezoidal approximation and is truncated at the probability corresponding to 10000-years. This yields the unique EAD value that represents the risk of flood in the catchment. By choosing an off-set value of probability for the integral and excluding the area subtended before this point, the resulting risk will account for assumptions on no-damage return period floods. This procedure was employed by Winsemius et al. (2013) and Ward et al. (2013) to account for the fact that low return period floods cause limited damages in the surrounding of

the channel and to include the presence of flood defences, by assuming that for a certain return period the flood wave will be constricted in the channel. In this study, a 2-years bankfull assumption was used to describe the channel geometry in the hydrodynamic domain (§ 2.4.2.). Because of this, the lower bound of the risk integral is set to the probability corresponding to a 2-years return period, assuming that no damage will occur for floods with a higher probability. To avoid including artefacts in the results when the simulation includes the presence of any level of defence (Prot10 to Prot1000), risk is calculated using the same lower bound instead of setting off the integral at the defence level assumed. This will ensure a homogeneous treatment of the results and consistency between the scenarios.

It should be noticed that for the current scenario both the 2UP dataset and the vulnerability estimates used represent a snapshot in time, corresponding respectively to 2010 and 2005 (Huizinga et al., 2017; Van Huijstee et al., 2018). However, in this study they are assumed to be representative of the whole timeseries of 1960-2000, potentially leading to an overestimate of damage if one considers the development that occurred since the beginning of the study period. Regardless, this error does not affect the answer to the RQs and is therefore considered acceptable.

3. Model validation

This chapter aims to provide a description of the performance achieved with GLOFRIM for this study. As the model performance influences the results of the study but is not the focus of the research questions, the validation is given a separate chapter from the results. The input data and parameters detailed here are used in all the simulations in order to obtain consistent results; hence, the model performance assessed here remains constant throughout the study. The validation run covers the study period of 40 years, from 01.09.1960 to 31.08.2000. For PCR-GLOBWB, a resolution of 30 arcminutes is chosen to restrain the computational effort and the wall clock runtime. For the same reason, the simple flux accumulation solver for the routing scheme is employed for PCR-GLOBWB, outside the coupled domain[8]. The model offers a fixed time-step of one day, whereas the adaptive time step of Lisflood is automatically activated with the sub-grid channel solver to improve the overall stability (Neal, Schumann, et al., 2012). GLOFRIM was configured to update the sub-grid channel discharge of Lisflood with the runoff and discharge fluxes of PCR-GLOBWB, and the River-Floodplain-Scheme was activated by exchanging variables with the most upstream sub-grid channel cell, as it was deemed beneficial for runtime (Hoch, Neal, et al., 2017).

3.1. Discharge series

The setup of GLOFRIM is evaluated against discharge observations and benchmarked against the results of PCR-GLOBWB alone. Pearson's correlation coefficient r and the Kling-Gupta Efficiency (Gupta et al., 2009), hence forward KGE, where chosen to assess the models' performance. In general, the correlation coefficient represents the ability of the model to match an observed pattern; as r approaches 1, the observations and simulated values will have a closer linear association. The KGE was especially developed for statistic interpretation of hydrological measurements; it incorporates r and the parameters of bias and variability, comparing respectively the mean value and standard deviation of the two datasets, allowing for a more insightful interpretation of the results.

Puttershoek and Lobith are chosen to compare the observed and simulated time series. These positions represent respectively the terminal branch of the river connecting the Waal to Rotterdam (the Oude Maas), and the point in the Rhine before flow is bifurcated in the Waal and Lek (Figure 8). At Lobith, the 40 years of observations between 01.09.1960 and 31.08.2000 are obtained from the original data[9] of the Global Runoff Data Centre (GRDC). At Puttershoek, only four years of the series, between 01.01.1997 and 31.08.2000, are available[10] from the website of the Dutch Ministry of Water Management and Infrastructures. Table 2 showcases the values obtained for Pearson's r and KGE at the two validation points, compared to the described datasets.

[8] Further information on the inputs of the model can be found in Sutanudjaja et al. (2018) and van Beek & Bierkens (2009)
[9] Dataset published 2018 via the Global Runoff Data Centre. Mean observed daily discharge at Lobith (GRDC no: 6435060), Rhine river in m3/s. The Global Runoff Data Centre, 56068 Koblenz, Germany. Available at: https://data.4tu.nl/repository/uuid:5de7c3c3-c22b-43d8-bc71-71913f6a3d23
[10] Available at: https://www.rijkswaterstaat.nl/water/waterdata-en-waterberichtgeving/waterdata

Table 2: Validation results: values of Parson's correlation and Kling-Gupta efficiency on discharge.

Validation point	Model set-up	Pearson's r	KGE
Lobith	Coupled hydrologic-hydrodynamic GLOFRIM run	0.78	0.45
	Hydrologic model PCR-GLOBWB in stand-alone mode, sub grid schematization of overbank storage active	0.73	0.6
Puttershoek	Coupled hydrologic-hydrodynamic GLOFRIM run	0.41	0.35
	Hydrologic model PCR-GLOBWB in stand-alone mode, sub grid schematization of overbank storage active	0.38	0.27

The better global trends at Lobith with respect to Puttershoek show that the model is more representative in the upstream section of the river network. A reasonable explanation for this is that the Dutch section of the Rhine and particularly its main branch – the Waal – is a highly engineered river course with a multitude of channels of different dimensions that drain and divert water to account for agricultural, navigation and other water management purposes. In addition to this, the flow bifurcates at two points, between the Maas and the Nederrijn and at the Ijssel branching. Such complexity is not grasped by the relatively simple channel network represented by the model, which as a result is more flawed the more downstream is the point used for comparison. The model not being able to appreciate these characteristics of the system does not imply a poor hydrodynamic performance, as confirmed by the accuracy showcased at Lobith.

If the results are benchmarked with the discharge simulated by PCR-GLOBWB, it can be observed that the correlation coefficient is consistently higher when the models are coupled, signifying that the more advanced routing scheme of Lisflood reacts more promptly to positive and negative changes in the water volumes fed to the system, as the plots overlay on the rising and receding sides of discharge peaks (Fig 11.a). The values of KGE lack the same consistency and offer different trends at the two validation points. At Lobith, the coupled models yield a lower overall efficiency, which indicates that the bias and variability are offset from the observations. As it can be noticed from Fig 11.a, this stems from the values simulated for peak discharges, which in many cases are comparatively higher; this overestimation is consistent with the results found by Hoch, Neal, et al. (2017). As addressed in the study, a possible attribution for this is that the configuration of GLOFRIM does not allow for a bi-directional coupling, where hydrologic variables are updated using the hydrodynamic outputs in a full feedback loop. Therefore, the volume of water entering the floodplain is not affected by processes such as evapotranspiration, and

the total discharge might be overestimated as consequence. At Puttershoek, GLOFRIM features better KGE values than PCR-GLOBWB. The reason is that PCR-GLOBWB routs the water along the direction of a specified local drainage network; given the coarse resolution of 30 arcmin, the Dutch section of the Rhine which bifurcates in two branches is only represented as a single channel. Therefore, outside this main route, discharge is generally underestimated (Fig 11.b); the higher resolution and sub-grid configuration of GLOFRIM allow to bypass this issue, as demonstrated by the higher efficiency value.

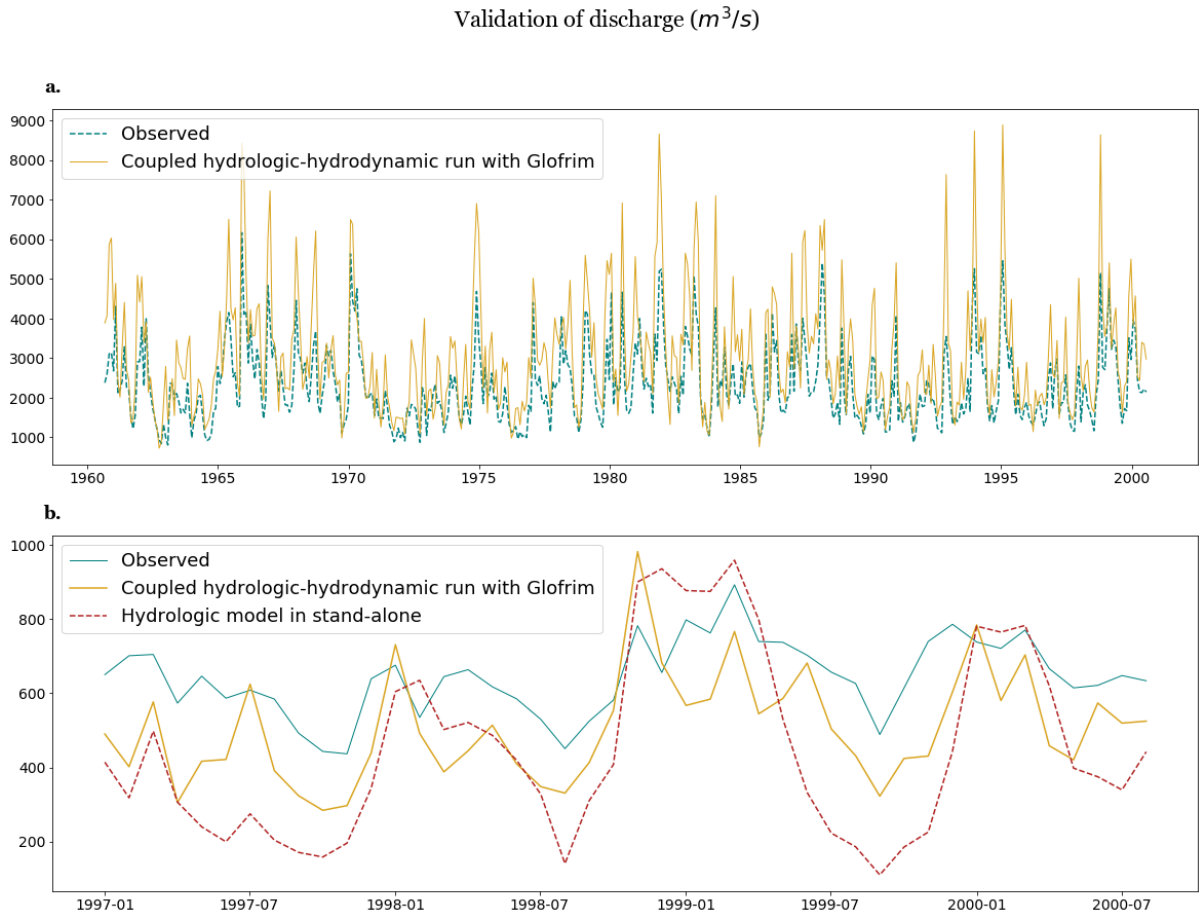

Figure 11: Validation plot of monthly averaged values ***a****. for entire study period, comparing the model with observations at Lobith* ***b****. for the period 1997-01-01 to 2000-09-01, comparing the model with observations and benchmarking the results with those of the hydrological model in stand-alone mode at Puttershoek.*

4. Results and discussion

In this chapter, first the results of the flood hazard analysis (sub-question a.) are presented following the methodology outlined under Step 1 (§ 2.5.). The results of two methods which have been developed to estimate the flood hazard are analyzed here. As discussed, the first method is based on the statistical extrapolation of flood depth values from the 40-year timeseries of historical climate. The second method is based off of the simulation of single events through the use of design hydrographs. The annual maximum discharge values at Lobith (from the statistical method) are analyzed first; then, the propagation of the flood wave (from the single event-simulation method) is observed. The inundation depth relative to the target return periods (2, 5, …, 1000) in the downstream part of the basin is then discussed, providing a term of comparison between the two methods. The flood depth also forms the basis for analysis of the flood risk (sub-question b.) following the methodology outlined under Step 2 (§ 2.6.) for which the results are presented and discussed next. This chapter concludes with the potential benefits and constraints to the applicability of the methods in other regions in future flood risk studies, after which the limitations encountered in the research are outlined and discussed.

4.1. Flood hazard

4.1.1. Statistical interpretation of discharge

A statistical analysis of the 40-year simulations obtained using the GLOFRIM framework yields information on the river flow condition and its changes across the different scenarios for varying upstream flood protection levels (0, 10, 50, 250, 500 and 1000 years). This sub-section focuses on the analysis of these trends.

Derivation of the annual maximum series at Lobith

Flow duration curves (FDCs) can be obtained from the six discharge series (Base to Prot1000) by considering the cumulative frequency of exceedance of discrete discharge values. With different protection levels, the curves show parallel but slightly different shapes for exceedance frequencies greater than 0.10 [-] (Fig 12). For less frequent events (exceedance frequencies of less than 0.10 [-]), corresponding to more extreme flow, the scenarios start to deviate. This is a direct consequence and demonstration of the effect of increasing protection levels in the upper part of the basin on discharge downstream. In fact, low flows are affected to a smaller extent as they hardly produce any inundation, and even little (or absent) protections upstream are sufficient to constrain the wave. The situation changes drastically for more extreme events (values below the threshold of 0.10 [-]): low levels of protection produce allow for overbank flow upstream and 'top off' the wave; high protection levels impede flooding upstream and as consequence discharges are higher at Lobith.

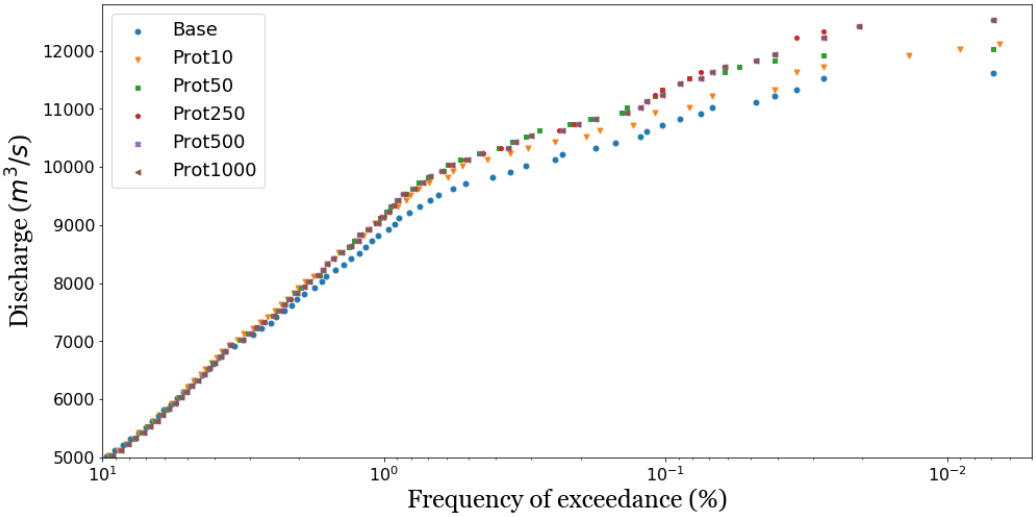

Figure 12: Changes in flow duration curves at Lobith for the different scenarios.

Extrapolation of the discharge at Lobith

As seen, the effect of protection levels influences the discharge values in the lower range of frequency of exceedance; this will reflect on the annual maximum series that can be derived from the simulated flow over the 40-year period at Lobith. In order to appreciate this change in magnitude of the events, 40 annual maxima are extracted from each scenario and used to fit a Gumbel distribution. Figure 13 is a plot of the Gumbel distributions with the confidence intervals of 95% on the regression.

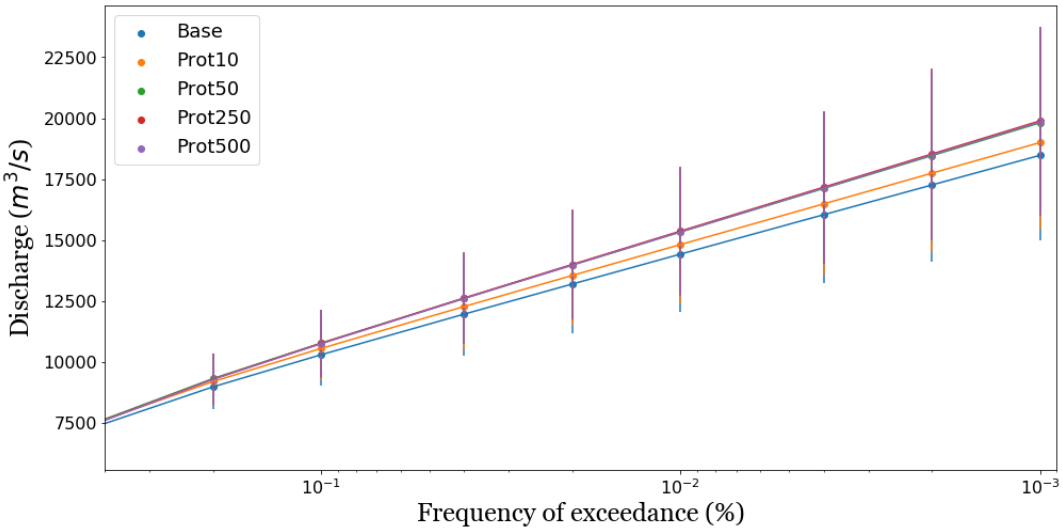

Figure 33: Extrapolation of the extreme values of discharge beyond the limit of the FDCs. The maximum value corresponds to a return period of 1000 years. The vertical bars indicate the confidence interval at each point for a confidence of 95%.

Table 3 shows the values obtained of the correlation coefficient (R^2) of the linear regression. The procedure to obtain R^2 and the confidence is described in Appendix C. Noticeably, the regression has

roughly the same level of goodness-of-fit throughout the different scenarios, in all cases close to 0.73. Despite these overall good values, by looking at the plots one can see that the confidence intervals often overlap between different scenarios.

Table 3: Goodness-of-fit of the annual maxima distribution with the Gumbel equation.

Scenario	Base	Prot10	Prot50	Prot250	Prot500	Prot1000
R^2	0.7328	0.7325	0.7315	0.7311	0.7312	0.7312

To explain this, it should be considered that any extreme values distribution will ideally represent a certain dataset with higher accuracy when the limit for the regression is close to the number of years in the sample. When the analysis is used to extrapolate values beyond this threshold, the results should be taken critically (Shaw et al., 2010). In our case, a 40-year time series is used to extrapolate values up to 1000 years of return period; this mismatch carries a large error for the higher range of return periods. This same limitation applies to the extrapolation of flood depth values and is further discussed below (§ 4.1.3.).

To quantify the effect visible from the plots, the relative discharge increase with comparison to the Base scenario can be considered. To this purpose, the nine return periods taken into account for this study can be associated to high- (2, 5, 10, 25 years), medium- (50, 100 years) and low-probability of occurrence (250, 500, 1000 years). The relative discharge increase is averaged for each of these three classes in Table 4. As can be observed for the values reported, the largest difference between the scenarios used for the comparison is found for events that fall under the low- and medium-probability classes. This highlights how the long-term hydrological behaviour of the river is changed by the presence of the defence measures with repercussions on a larger time scale than that of the simulations. Considering the stage-discharge relationship of the river, the increase in discharge found for low-frequency events, which reaches up to 7% of the current values, will translate into a rise of the associated water level.

Table 4: Increase of discharge by protection scenario with respect to the Base. The values are averaged within each probability class to represent the overall change for high-, medium- and low-probability of occurrence events.

Return period	High probability	Medium probability	Low probability
Relative discharge increase (%)			
Prot10	2.41	2.69	2.8
Prot50	3.91	6.1	6.96

Prot250	3.7	6.3	7.04
Prot500	3.56	6.11	7.11
Prot1000	3.56	6.11	7.11

4.1.2. Flood wave propagation

The simulation of single flooding events performed as discussed under Method B (§ 2.5.2.) allows to observe the characteristics of the flood wave and how these are affected by the protections upstream. Figure 14 shows the obtained hydrographs at Lobith for the 10- and 250-year return period events. The remaining curves for Lobith are shown in Appendix D.

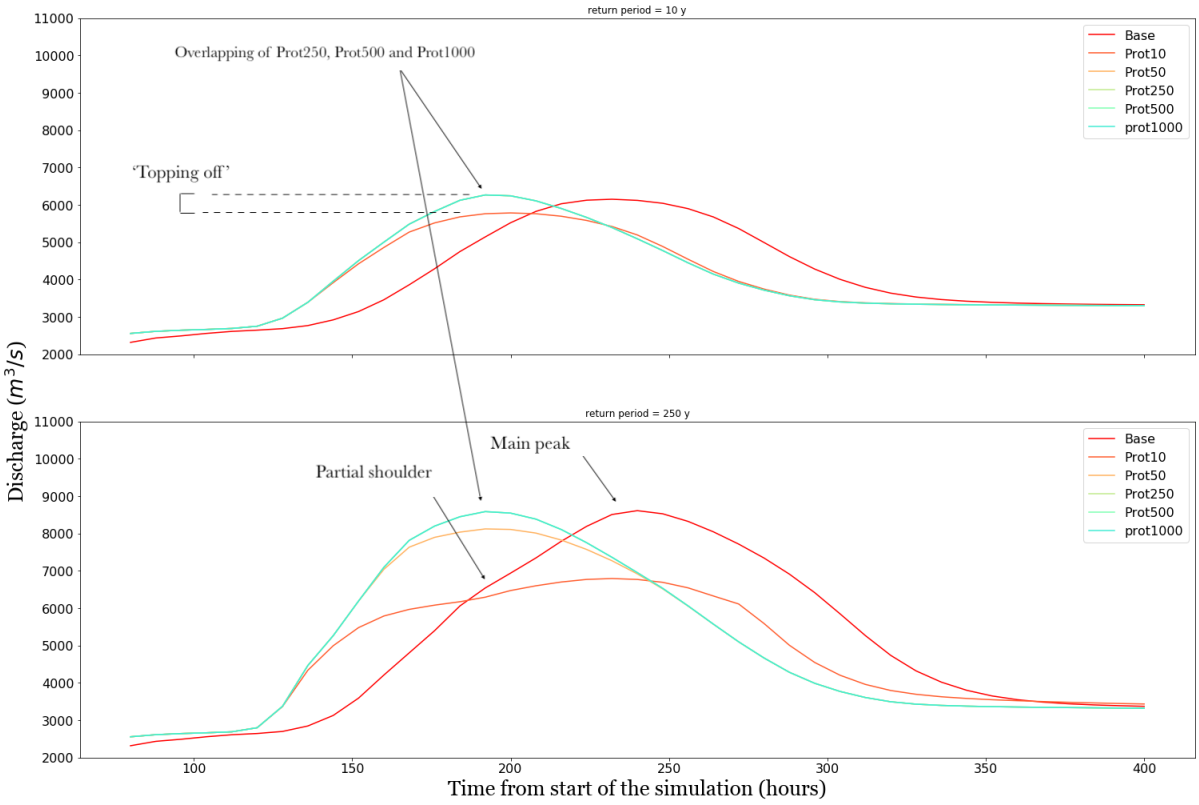

Figure 14: Hydrograph comparison between the six scenarios at Lobith. The two return periods of 10 and 250 years are shown, out of the nine simulated.

As consequence of the protection levels upstream, a separation between the same return period curves can be observed. From the profiles in the image, it can be noticed that the overall volume of water reaching Lobith changes when protections are applied upstream. In particular, the volume associated with higher

protection levels is larger. This can be observed by comparing Prot10 with Prot1000 in the 10 years event or Prot10 and Prot50 with Prot1000 in the 250 years event. The reason behind this is the 'topping off' effect that occurs when water is allowed to spill in the floodplain, when the embankments are smaller. The expectation for the volume in the unprotected scenario is to be the smallest in the series; however, it can be noticed that it is comparable to the high protection cases. A reasonable explanation is that in this scenario the overbank flow returns to the channel as there is no embankment to prevent this. This is confirmed by the partial appearance of a shoulder before the main peak. Overall, the effect that is observed on the FDCs is echoed by the behaviour of the flood wave at the scale of the single event, where higher protections upstream correspond to larger volumes of water reaching Lobith and the downstream section of the catchment.

It can be noticed that there is overlapping between the hydrographs for the scenarios Prot250, Prot500 and Prot1000 (noticeable also in the rest of the curves in Appendix D), which might indicate that the lower of these protection levels is sufficient to avoid overbank flow even considering a return period event of 1000 years. This effect can be described as a 'saturation' of the response signal of the catchment to the protection level assumed upstream, in that the results do not experience any changes above the threshold of Prot250. The reason behind this could be found in a mismatch between the height of the design hydrographs for the return periods (2, 5, …, 1000) and the height of the embankments. For the sake of simplifying the parametrization of the hydrodynamic domain and the characterization of the scenarios, the protection levels were uniformly based on the design discharges found at Lobith (§ 2.4.2.), whereas the hydrographs were based on the discharge at Bonn. Hence, the difference in discharge between these two points is large enough to have caused an overestimation of the height of the embankments for the two higher protections scenarios.

Another effect noticeable from the curves in figure 14 is that the offset of the event occurs earlier when protections are applied upstream. This is noticeable in a shift in time of the rising limbs and discharge peaks. To evaluate this effect for the entire catchment, discharge is monitored at five checkpoints positioned at 55, 160, 205 (Lobith), 245 and 325 km along the main channel (§ 2.4.2., Figure 8). As noticeable from Figure 14 (and Appendix D), the timing of the peak varies mostly with the scenario considered, rather than the magnitude of the event simulated. Therefore, the time to peak averaged across return periods is shown in Table 5.

Table 5: time of peak at different distances in the channel from the start of the simulation. The value given is the average for all return periods in the same scenarios.

Position (km)	**55**	**160**	**205 (Lobith)**	**245**	**325**
Mean time of peak arrival (hours)					
Base	176	200	240	272	328
Prot10	176	200	224	256	312
Prot50	168	176	184	232	296

Prot250	168	176	184	232	296
Prot500	168	176	184	232	296
Prot1000	168	176	184	232	296

When the measurement is taken downstream, at 245 or 325 km, the time gap between the base and the high protections scenarios increases with respect to the upstream measurements. This indicates that under the effect of embankments, the flow is characterised by a higher velocity. As result, in Rotterdam (close to km 325) the flood peak arrives 32 hours earlier if the highest defence is built in the upstream section. The time to peak (i.e. from the offset of the rising limb to the peak) of the synthetic hydrographs used in the simulation is roughly of 3 days. The simulation time needed for the peak to reach Rotterdam is 328 hours without protections. Subtracting these two values leaves an initial lead time of 10 days in Rotterdam. An anticipation of 32 hours implies that this time is reduced by more than 10%. The peak time anticipation found is not only substantial within this simulation, but also if compared to the maximum of 2 days of lead time for sophisticated early warning systems (Cools et al., 2016). The change in flood timing provokes an effect on flood risk that is not considered in strict monetary terms but will in general affect the capacity of flood response downstream and increase damage, as a consequence.

4.1.3. Flood distribution

The purpose of this paragraph is to discuss and compare the results obtained in terms of the depth and extent of the inundation with the two methods (statistical approach and single event-based) applied. Figure 15 gives an exemplifying illustration of the different hazard outcomes for the two methods and the administrative and aggregated (downstream and upstream) regions used for the analysis of hazard and risk.

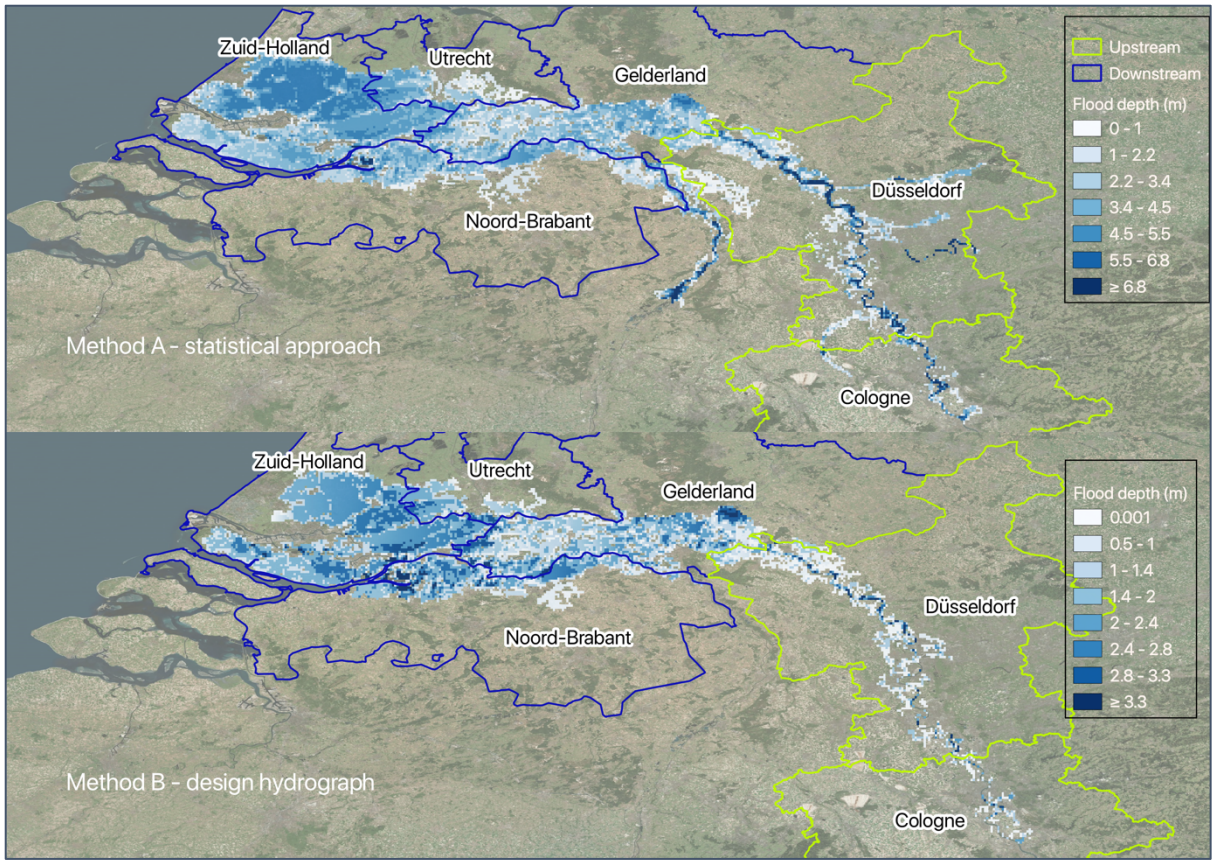

Figure 15: Administrative, upstream and downstream regions used to analyse the results. On the background, a 1000-year inundation taken from the Base scenario for method A (above) and B (below).

Flood depth

To see the effect of embankments on the inundation depth, the flood map of a specific return period (2, 5, …, 1000) in the Base scenario is subtracted from the corresponding return period map of all other scenarios (Prot10 to Prot1000). This gives the absolute change in water depth on a cell-by-cell basis. These values are averaged within the bounds of the upstream and downstream regions respectively, giving the mean flood depth change upstream and downstream. This analysis is applied to the hazard maps obtained through the statistical extrapolation (Method A) and through the design hydrographs (Method B). Figure 16 and 17 illustrate the results in boxplots for the two sections of the catchment and the two methods applied, respectively.

Considering the statistical approach first, both regions of the catchment experience a decrease of the (average) flood depth when the lowest protection level is applied. As the embankments become higher, this effect becomes almost non-existent downstream, while upstream the change becomes positive, i.e. floods become deeper at higher protections applied. At the same time, the average change downstream is neglectable in the overall catchment balance as the values are almost two orders of magnitude greater upstream in either direction (decrease or increase). The increasing flood depth upstream defies the expectation of a reduction of hazard where the protection is applied. A plausible explanation is that

because of the embankments, low return period floods are constrained in the channel and only high magnitude floods actually occur in the floodplain. Therefore, the statistical extrapolation does not 'see' the low (usually more frequent) values and is based on high magnitudes only. This could explain the bars on the boxes for Prot250, Prot500 and Prot1000, where the largest positive changes are associated to the lowest return periods.

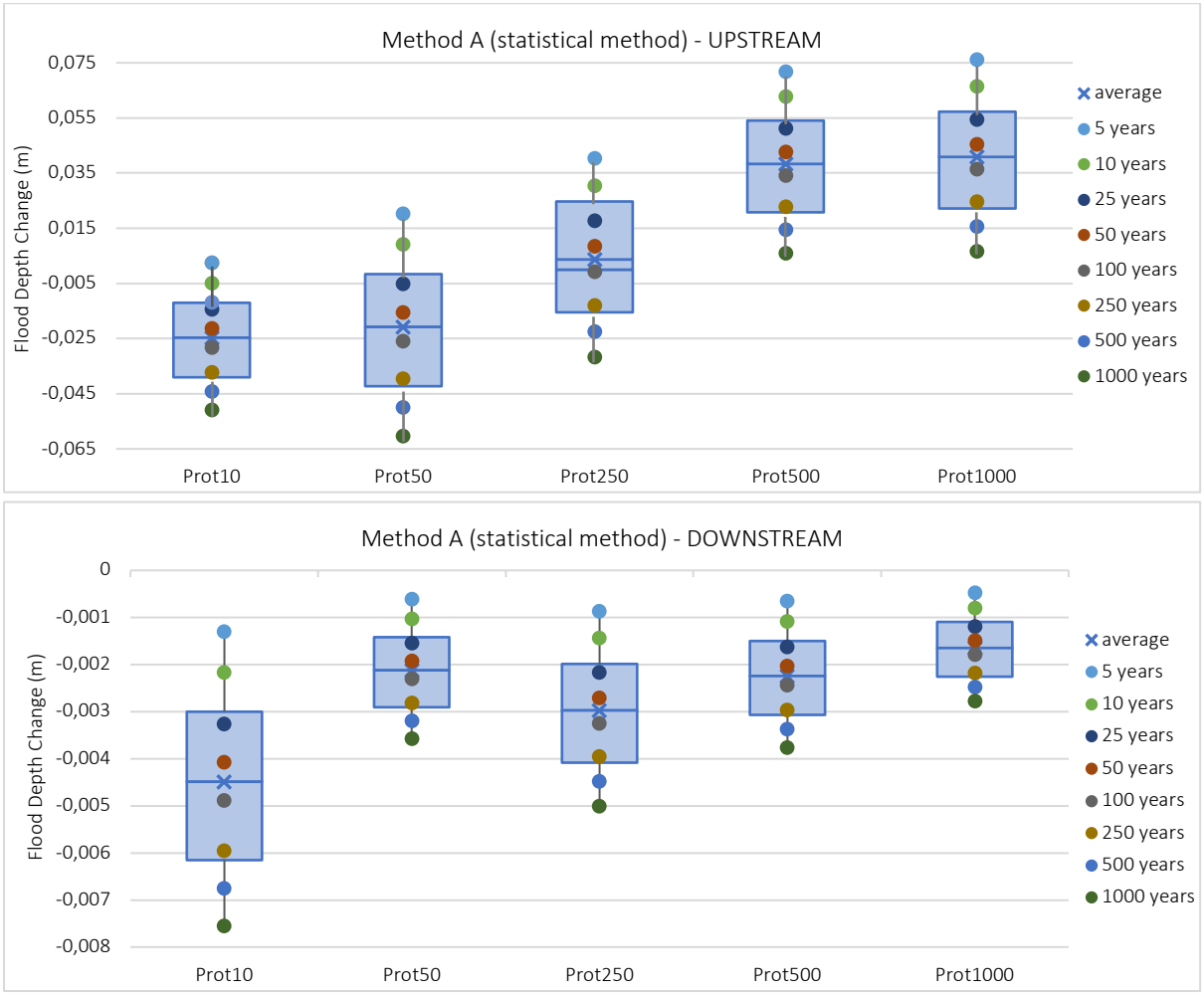

Figure 16: Boxplot of the increase of inundation depth with respect to the Base scenario. The two images refer to values obtained for the upstream (above) and downstream (below) regions. The bounds of each box refer to the first and third quantile relative to the return periods; the line in between refers to the median value across return periods. The points indicate the mean value per return period. These results belong to Method A (statistical extrapolation).

By looking at the values from the single-event simulations, a net decrease of flooding can be observed upstream, consistent with the increase of protection levels. For the region downstream, there is a symmetrical increase of the (average) flood depth, which could substantiate the hypothesis of a 'transfer' of the flood hazard from upstream to downstream occurring when protections are raised. The absolute value of the decrease upstream almost doubles the increase downstream. However, considering that the flooded region downstream is larger, the volume will be comparatively more spread.

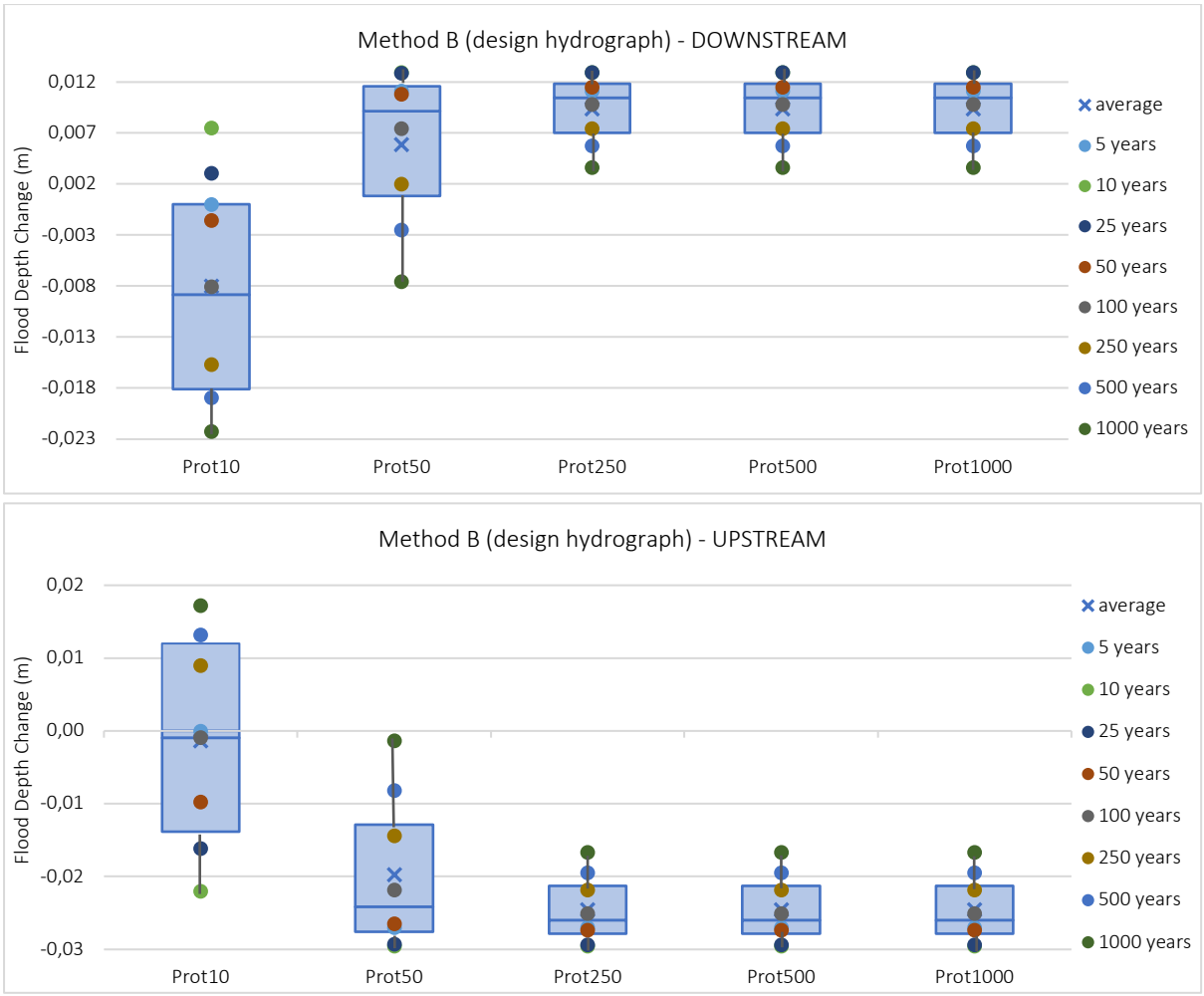

Figure 17: as figure 16 (above), with the difference that results are shown for Method B (design hydrograph).

Flood extent

The most visible difference between the two methods is in the simulated extent of the inundation. While simulating the single events starting from the design hydrograph changes the overall flooded surface, the statistical method applies the linear regression on all the cells that have experienced inundation on the 40-year time series. This produces an effective inundation on low return-period events even in conditions of high defence levels. From the comparison (Figure 18; Appendix D), it can be noticed how this creates an anomaly in the upstream catchment, where the event-based simulation does not provide flooding. On the other hand, the single event simulation underestimates contribution to the inundation from the tributaries. This effect is also present in the total volume of water entering the channel, which can be observed if one compares the peaks of the hydrographs at Lobith with the extrapolated values from the Gumbel analysis (Figure 14). This is because the average conditions were used outside the main channel, with the effect of underestimating the contribute of the lateral branches.

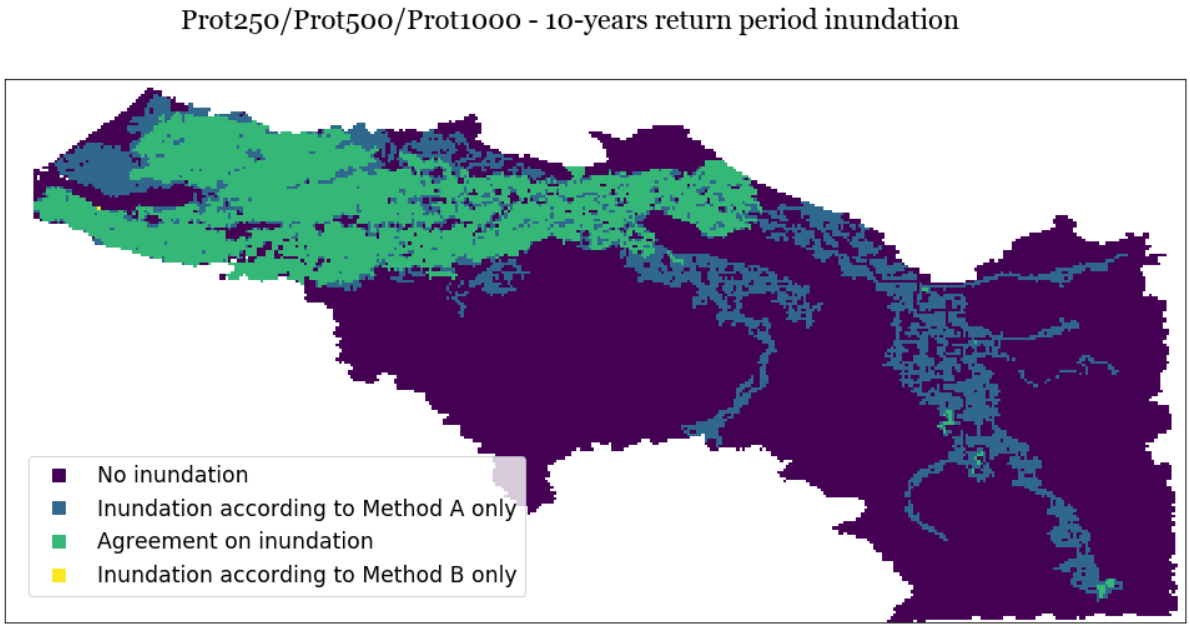

Figure 18: 10-years return period event in the three highest protection scenarios for both methods.

To explain the behaviour observed in the outcomes of the statistical approach, the annual maximum depth values from the 40-year time series are compared to the relative Gumbel fit to obtain an R^2 value for the linear regression on a cell-by-cell basis. As result, for every scenario in the statistical method, a spatial distribution of the coefficient of determination is retrieved. It can be noticed how the goodness-of-fit results in values between 0.5 and 0.6 [-] at the peripheral cells in the inundated domain and in the proximity of the embanked river section (Figure 20 a). These represent a step change from the average R^2 values in the map and take on the role of outliers (Figure 20 b).

According to the values in Table 6, this effect appears for all the protection scenarios, as the mean R^2 is always lower compared to that of the Base scenario. Worth of notice is also that the standard deviation taken on the average R^2 values is in general higher for all the scenarios when compared to the Base. This is another indication of the fact that the mean value of the correlation coefficient is lowered by the presence of outliers in the distribution. This corresponds with the presence of specific regions where the statistical method performs less accurately as the protection increases.

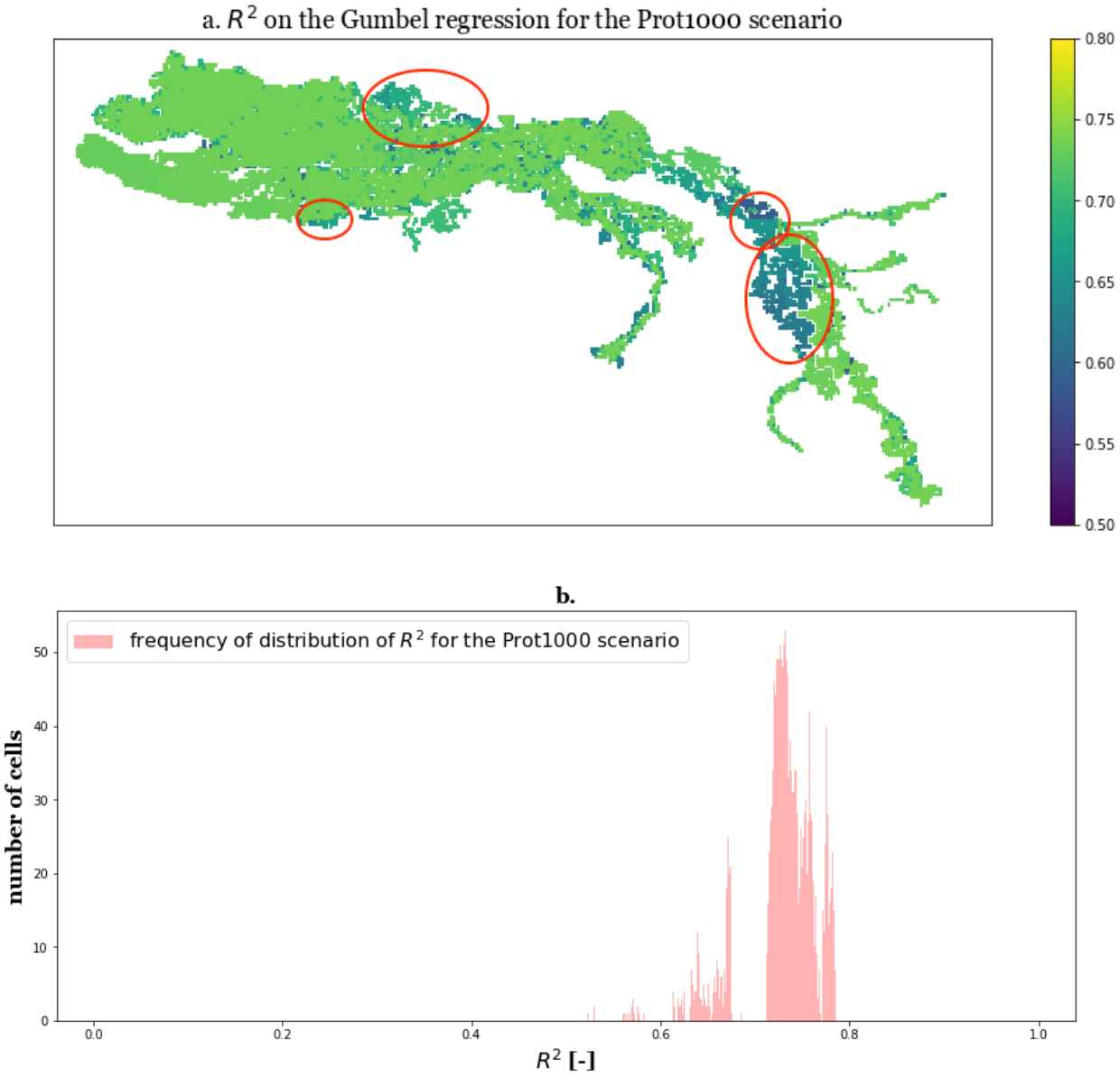

Figure 20: ***a****. goodness of fit for the cell-by-cell Gumbel regression analysis in the Prot1000 scenario. The distribution in the study area is show by taking into account the range of values 0.5 – 0.8 of* R^2 ***b****. The range was selected based on a cumulative histogram of the* R^2 *values found in all cells.*

Table 2: mean determination coefficient values for the Gumbel regression of all scenarios.

Scenario	Mean R^2	Standard deviation of R^2
Base	0.722	0.0287
Prot10	0.719	0.0314
Prot50	0.715	0.0388
Prot250	0.719	0.0343
Prot500	0.719	0.0347
Prot1000	0.720	0.0309

These values point out that the method has a low representativeness in those cells where there are only sporadic events with inundation. Consistently with these observations, a plausible explanation is that for few events during the 40-year time series, the water in the channel has overflown and travelled further in the floodplain due to the higher elevation potential of the raised topography, corresponding to the embankments. In these cases, the fitting is imposed on a sample of values that do not behave accordingly to an extreme values distribution, which causes the results to derive from an ill fitted extrapolation of depth maxima. This explanation is compatible with the findings for the flood depth in the previous paragraph. Ward et al. (2013) applied a lower threshold of at least 5 days of inundation per year, which might eliminate the cells featuring low values of correlation coefficient. However, this raises the question of what the optimal threshold is to apply in the analysis, to avoid the loss of important features in the flood map. Furthermore, in this study the statistical extrapolation is applied on a higher resolution (30 arcseconds) with respect to previous attempts (2-5 arcminutes in Feyen et al., 2010; Ward et al., 2013; Winsemius et al., 2013). This, as demonstrated by the effect produced through raising the embankments, enhances the effect of low-scale topographical features and increases the chances of cells with low correlation values. This might indicate that there is a lower limit to the resolution at which the statistical method can be applied.

4.2. Flood risk

From the series of return period hazard maps, the EAD can be calculated following the methodology described under § 2.6. From the two hazard assessment methods, two series of risk outcomes are obtained. The total EAD obtained per administrative region is given in Fig 21 and 22 (for Method A and B) and compared across scenarios. The results obtained from the statistical approach reflect in large part what was observed in the flood depth analysis. In fact, with comparison to the Base scenario, the regions that make up the downstream section do not experience a significant change in the EAD. Across all scenarios, the most significant change occurs because of a reduction of risk in Cologne and Düsseldorf at the two lowest levels of protection (Prot10 and Prot50). For higher protections, both regions perceive an increase of EAD related to the low R^2 cells discussed above (§ 4.1.3.).

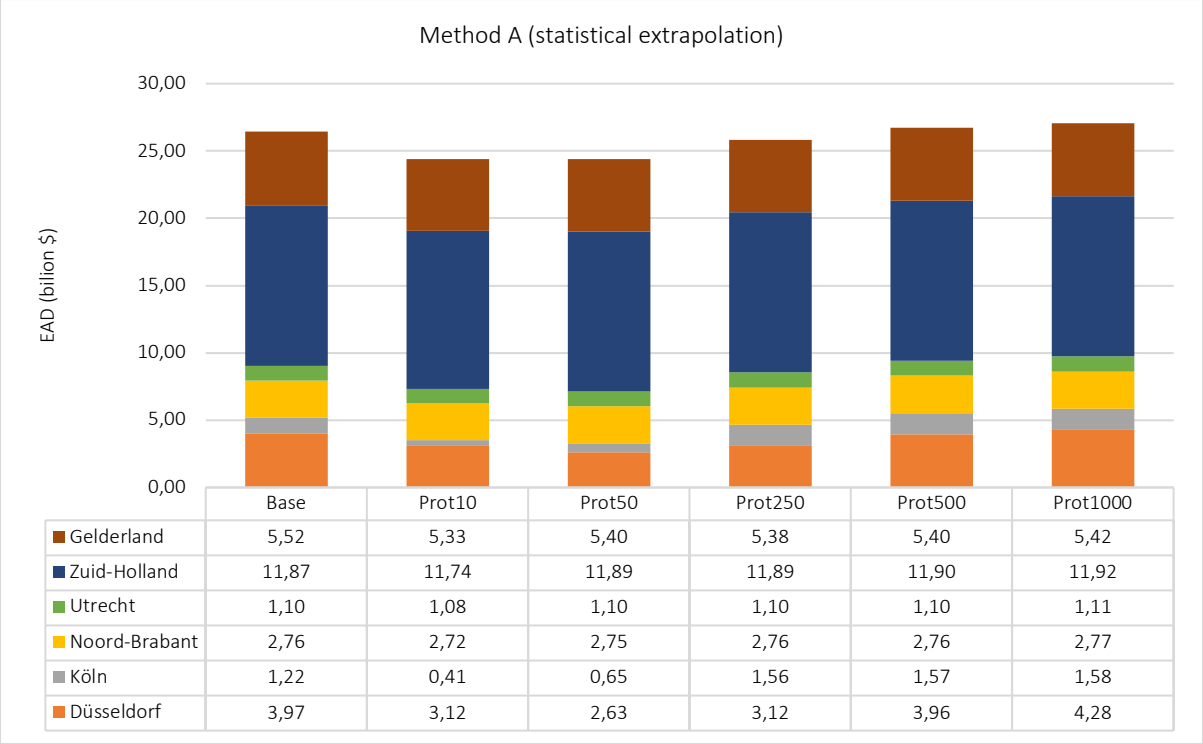

	Base	Prot10	Prot50	Prot250	Prot500	Prot1000
Gelderland	5,52	5,33	5,40	5,38	5,40	5,42
Zuid-Holland	11,87	11,74	11,89	11,89	11,90	11,92
Utrecht	1,10	1,08	1,10	1,10	1,10	1,11
Noord-Brabant	2,76	2,72	2,75	2,76	2,76	2,77
Köln	1,22	0,41	0,65	1,56	1,57	1,58
Düsseldorf	3,97	3,12	2,63	3,12	3,96	4,28

Figure 21: stacked histogram of the EAD values found for each administrative region in all scenarios. The results in this image are obtained from the hazard maps of Method A (statistical extrapolation).

The single event simulations show a recognizable pattern related to the overall increase in EAD of the catchment with higher protection levels in place (Figure 22). With respect to the other method, the risk of flooding in the two regions upstream (Cologne and Düsseldorf) is only a small fraction of the total damage experienced in the catchment. Although these regions show a decreasing risk (consistent with the decrease of flood depth), the absolute value of the change is irrelevant with comparison to the increase experienced by the aggregate of the four regions downstream. In particular, the region of Zuid-Holland has the highest initial value of EAD and the highest (absolute and relative) overall increase. This implies that the transfer of risk from the upstream catchment is localized and not uniform throughout the downstream region. It could be explained considering that the speed of the wave propagation was higher with the highest protection scenarios considered, resulting in the flood propagating further in the domain. In fact, the risk aggravation occurs in Zuid-Holland and Utrecht, which are the most downstream regions, while Gelderland and Noord-Brabant, closer to the upstream section, experience a reduction in EAD.

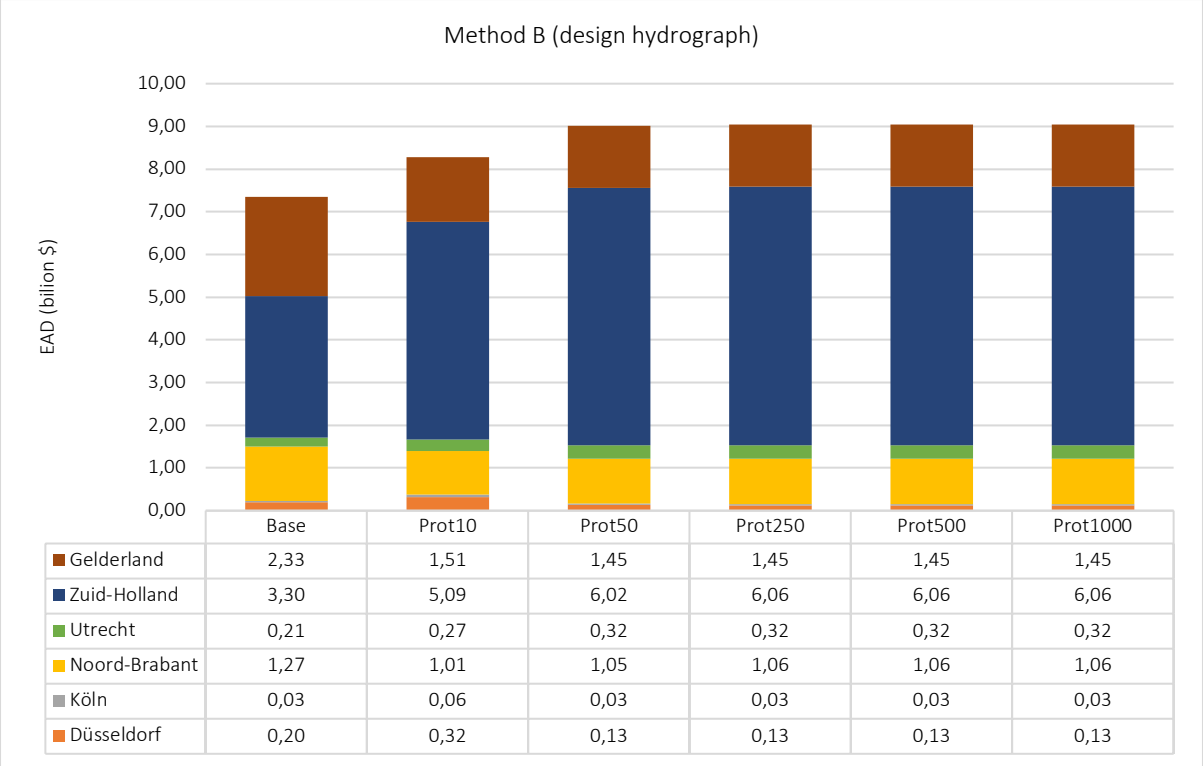

	Base	Prot10	Prot50	Prot250	Prot500	Prot1000
Gelderland	2,33	1,51	1,45	1,45	1,45	1,45
Zuid-Holland	3,30	5,09	6,02	6,06	6,06	6,06
Utrecht	0,21	0,27	0,32	0,32	0,32	0,32
Noord-Brabant	1,27	1,01	1,05	1,06	1,06	1,06
Köln	0,03	0,06	0,03	0,03	0,03	0,03
Düsseldorf	0,20	0,32	0,13	0,13	0,13	0,13

Figure 22: Same as figure 21 (above), with results from method B (design hydrograph)

Comparing the two methods, there is a large difference with the overall risk outcome, as the statistical approach finds systematically larger values for all the regions considered. This is explained by higher values of flood depth found with this method, as can be seen from the hazard comparison for one scenario in Figure 15. In addition, the inter-regional comparison shows that there is more variability in the outcomes of the single simulations, while Method A gives more comparable regional EADs. This observation can be explained by the fact that the flood extent changes more dynamically with the single simulations, while the statistical approach finds different depth values in a fixed inundation extent. Therefore, the different extent can affect parts of the region that were previously not flooded, changing the exposure to the flooding event.

A direct answer to sub-question b. can be found by comparing the aggregate values for the upstream and downstream regions (Table 7). Both methods find an upward trend in the total risk of the catchment when protections are applied upstream. However, for the statistical extrapolation this is a result of risk increase upstream, that is subject to the considerations on the representativeness of the method carried on in the hazard discussion (§ 4.1.3.). The results of the single event simulations present a coherent picture of flood risk increase in the downstream region correlated with a decrease upstream. Moreover, the damage experienced downstream offsets considerably the reduction of damage for the upstream region, as consequence of the presence of embankments. The overall EAD inflicted by the presence of embankments can be evaluated, according to these outcomes, in between 0.9 and 1.7 billion $ for the entire catchment.

Table 7: comparison of the avoided and inflicted EAD between each scenario and the Base scenario.

Scenario	EAD change upstream	EAD change downstream	**Total EAD change**
Method A: EAD (billion $)			
Prot10	-1.66	-0.37	**-2.03**
Prot50	-1.91	-0.12	**-2.03**
Prot250	-0.51	-0.12	**-0.63**
Prot500	+0.33	-0.08	**0.26**
Prot1000	+0.65	-0.04	**+0.63**
Method B: EAD (billion $)			
Prot10	+0.15	+0.78	**+0.92**
Prot50	-0.07	+1.73	**+1.66**
Prot250	-0.08	+1.76	**+1.69**
Prot500	-0.08	+1.76	**+1.69**
Prot1000	-0.08	+1.76	**+1.69**

4.3. Applicability of the results

The results of this research demonstrate that the effect of embankments upstream generates an increase of flood risk for the entire catchment. For the Netherlands, a river flood risk assessment of the future climate found between 0.3 and 3.3 billion € between the least and most extreme scenario (Feyen et al., 2010). The most extreme EAD change found in this study for the same region (taken as the downstream region) fits in the higher half of this range, implying that the increase of risk is comparable to that provoked by long-term anthropogenic alterations of the general climate. However, while this acts on the river hydrology in the course of decades, with estimates being made for the mid- or end-century (Feyen et al., 2010; Hirabayashi et al., 2013), the construction of embankments is measured in terms of years (Scussolini et al., 2016). As such, it can provoke a step-change in the risk of flood that is otherwise associated with the long-term behaviour of the river. The most immediate consequence of this is that the flood defences downstream become obsolete or less effective on the same flood frequencies that they were designed for. This effect should be included in large-scale studies as in can significantly change the risk estimates for a region and the cost-benefit analysis associated with flood protections of embankment type (Ward et al., 2017).

A critical step in the achievement of this level of analysis is that flood protections are represented as features of the modelled domain and not through post-processing; this is no trivial task when one considers

the large or global scale at which these studies aim to be applied (Ward et al., 2015). The issues of accuracy evidenced here with the statistical method are inherent with 'burning' the embankments in the elevation features of the DEM, an expedient that works only when the resolution is below the size of the feature (Wing et al., 2019) or, as shown here, with single-event simulations. Trying to improve the representativeness of the statistical method (especially upstream), for instance through a cell-based ruling-out procedure on the basis of the goodness-of-fit, is not envisaged as solution to this. In fact, the results of this research evidenced that the statistical extrapolation finds no change of hazard or risk downstream, even though the design hydrographs proved this effect. At the same time, using design hydrographs to construct the EPL curve at the global scale, as it is currently in the capability of global models, or even just large regions would be a time-consuming process involving a degree of arbitrariness, non-automatization and without the guarantee of satisfactory results. For instance, long-term time series or the effect of combined events on large catchments go unrepresented.

For models where the channel flow is separated from the floodplain, a possible way forward to include the embankments at the level of physical representation is to introduce a parameter in the model to account for the increased channel conveyance given by the flood protection. This would include the physical effect of embankments without the need to manipulate the low-resolution DEM. Once implemented, it could allow for the use of the statistical method on long-term series and large (regional to global) spatial domains. At the same time, the results have implications even for spatial domains within the catchment boundaries where a more sophisticated representation of the embankments is desirable, for instance when design flood levels need to be assessed. In this case, the flood protection should be included as terrain features using for instance the automated detection algorithm of Wing et al., (2019).

4.3.1. Limitations

The issues with the parametrization of GLOFRIM have been discussed in the validation of the model; the most noticeable one is that the peak discharges are overestimated. This gives a systematic overestimation of the annual maximum series that are used to provide the Gumbel regressions for discharge. This problem could be overcome in future studies with the two-directional coupling of GLOFRIM. An issue of the method noticed and discussed in the results is that of the 'saturation' effect of the risk outcome for the three highest protection levels applied. A uniform hight of the embankments was assumed for the upstream catchment, which led to overestimating the defence levels with respect to the design floods. In future studies, this could be accounted for by computing the embankment height from the channel section at each cell of the 1D river domain. An additional gain in the quality of the method would be achieved by using a longer series of climatic inputs. In fact, as noted in the results, this should be as close as possible to the highest extrapolated magnitude. The 40-year series used here does not allow to surmount a value of correlation coefficient in the range of 0.73 [-] for the discharge and flood depth series. Finally, errors are also generated in the damage assessment part of the methodology; as discussed previously in Tiggeloven et al. (2020), the main limitation in the inputs used for the vulnerability

curves is that all the assets are grouped in three types and the vulnerability is assumed equal within each type. The error on the damage assessment has perhaps a lower specific weight here, considering that it is constant across the scenarios considered and as such it does not compromise the quality of the comparison.

5. Conclusion

The aim of this research is to evaluate the effect of river embankments on the propagation of flood risk in a catchment. To this purpose, a parametric analysis was designed, where the flood protections in the upstream section of a catchment were used as variable to see the effect on the distribution of risk. From the perspective of hazard, the embankments were found to affect the frequency-magnitude relationship for the discharge in the channel, namely by increasing the extreme values associated with a certain return period. At the same time, the travel time of the wave in the catchment decreased as the embankments were raised upstream, decreasing the available time to activate flood response mechanisms. As two methods were used to assess the depth and extent of the inundation associated with a predefined range of return periods, it was found that the first method, which is frequently used in large scale flood risk assessment studies, did not capture the effect of protections. The hazard and risk metrics computed with this method did not change significantly for the downstream section of the catchment, while they increased in the upstream region as the protections where raised. The second method used, instead, fulfilled the initial expectations as the overall risk increased downstream, in conjunction with a reduction upstream. Moreover, the aggregated risk for the entire catchment was increased by all levels of protection.

Overall, the effect of the embankments was found to be substantial and to aggravate the conditions for flood risk. Large scale risk assessment models should be able to incorporate this level of analysis for the effect of flood protections, whereas now the 'positive' effect alone is considered. Therefore, the way forward necessitates to include an improvement of the representation of these small-scale elements in large scale simulations, which will only be achievable at the level of the model's engine.

Bibliography

Alfieri, L., Bisselink, B., Dottori, F., Naumann, G., de Roo, A., Salamon, P., Wyser, K., & Feyen, L. (2017). Global projections of river flood risk in a warmer world. *Earth's Future*, *5*(2), 171–182. https://doi.org/10.1002/2016EF000485

Andreadis, K. M., Schumann, G. J. P., & Pavelsky, T. (2013). A simple global river bankfull width and depth database. *Water Resources Research*, *49*(10), 7164–7168. https://doi.org/10.1002/wrcr.20440

Bates, P. D., & De Roo, A. P. J. (2000). A simple raster-based model for flood inundation simulation. *Journal of Hydrology*, *236*(1–2), 54–77. https://doi.org/10.1016/S0022-1694(00)00278-X

Bates, P. D., Horritt, M. S., & Fewtrell, T. J. (2010). A simple inertial formulation of the shallow water equations for efficient two-dimensional flood inundation modelling. *Journal of Hydrology*, *387*(1–2), 33–45. https://doi.org/10.1016/j.jhydrol.2010.03.027

Botzen, W. J., & van den Bergh, J. C. J. M. (2012). Monetary valuation of insurance against flood risk under climate change. *International Economic Review*, *53*(3), 1005–1026.

Braun, B., & Aßheuer, T. (2011). Floods in megacity environments: Vulnerability and coping strategies of slum dwellers in Dhaka/Bangladesh. *Natural Hazards*, *58*(2), 771–787. https://doi.org/10.1007/s11069-011-9752-5

Ceola, S., Laio, F., & Montanari, A. (2014). Satellite nighttime lights reveal increasing human exposure to floods worldwide. *Geophysical Research Letters*, *41*(20), 7184–7190. https://doi.org/10.1002/2014GL061859

Clerc, S. Le, Sauquet, E., & Lang, M. (2003). *Scaling properties of flood hydrographs and their use to derive design flood hydrographs. 60.*

Clilverd, H. M., Thompson, J. R., Heppell, C. M., Sayer, C. D., & Axmacher, J. C. (2016). Coupled Hydrological/Hydraulic Modelling of River Restoration Impacts and Floodplain Hydrodynamics. *River Research and Applications*, *32*(May), 1927–1948. https://doi.org/10.1002/rra.3036

Cools, J., Innocenti, D., & O'Brien, S. (2016). Lessons from flood early warning systems. *Environmental Science and Policy*, *58*, 117–122. https://doi.org/10.1016/j.envsci.2016.01.006

Criss, R. E., & Shock, E. L. (2001). Flood enhancement through flood control. *Geology*, *29*(10), 875–878. https://doi.org/10.1130/0091-7613(2001)029<0875:FETFC>2.0.CO;2

De Moel, H., Aerts, J. C. J. H., & Koomen, E. (2011). Development of flood exposure in the Netherlands during the 20th and 21st century. *Global Environmental Change*, *21*(2), 620–627. https://doi.org/10.1016/j.gloenvcha.2010.12.005

De Moel, H., Bouwer, L. M., & Aerts, J. C. J. H. (2014). Uncertainty and sensitivity of flood risk calculations for a dike ring in the south of the Netherlands. *Science of the Total Environment*,

473–474, 224–234. https://doi.org/10.1016/j.scitotenv.2013.12.015

de Wit, K. M., & Buishand, A. (2007). *Generator of Rainfall And Discharge Extremes (GRADE) for the Rhine and Meuse basins*. http://www.verkeerenwaterstaat.nl/kennisplein/3/6/360696/RR2007.027.pdf

Di Baldassarre, G., Castellarin, A., & Brath, A. (2009). Analysis of the effects of levee heightening on flood propagation: example of the River Po, Italy. *Hydrological Sciences Journal*, *54*(6), 1007–1017. https://doi.org/10.1623/hysj.54.6.1007

Di Baldassarre, G., Viglione, A., Carr, G., Kuil, L., Salinas, J. L., & Blöschl, G. (2013). Socio-hydrology: Conceptualising human-flood interactions. *Hydrology and Earth System Sciences*, *17*(8), 3295–3303. https://doi.org/10.5194/hess-17-3295-2013

Economidou, M., Atanasiu, B., Despret, C., Maio, J., Nolte, I., Rapf, O., Laustsen, J., Ruyssevelt, P., Staniaszek, D., & Strong, D. (2011). Europe's buildings under the microscope. A country-by-country review of the energy performance of buildings. *Buildings Performance Institute Europe (BPIE)*, 35–36.

Eilander, D., Hoch, J. M., Ikeuchi, H., & Baart, F. (2018). GLOFRIM 2.0: coupling hydrologic and hydrodynamic models across scales for improved flood simulations. *AGU Fall Meeting Abstracts*, *2018*, H33S-2315.

Feyen, L., Dankers, R., Bódis, K., Salamon, P., & Barredo, J. I. (2010). Fluvial flood risk in Europe in present and future climates. *Journal of Geophysical Research Atmospheres*, *114*(16), 47–62. https://doi.org/10.1029/2008JD011523

Gumbel, E. J. (1941). The return period of flood flows. *Anna. Math. Stat.*, *12*(2), 163–190.

Gupta, H. V., Kling, H., Yilmaz, K. K., & Martinez, G. F. (2009). Decomposition of the mean squared error and NSE performance criteria: Implications for improving hydrological modelling. *Journal of Hydrology*, *377*(1–2), 80–91. https://doi.org/10.1016/j.jhydrol.2009.08.003

Heine, R. A., & Pinter, N. (2012). Levee effects upon flood levels: An empirical assessment. *Hydrological Processes*, *26*(21), 3225–3240. https://doi.org/10.1002/hyp.8261

Hijmans, R., Garcia, N., & Wieczorek, J. (2010). *GADM: database of global administrative areas*.

Hirabayashi, Y., Mahendran, R., Koirala, S., Konoshima, L., Yamazaki, D., Watanabe, S., Kim, H., & Kanae, S. (2013). Global flood risk under climate change. *Nature Climate Change*, *3*(9), 816–821. https://doi.org/10.1038/nclimate1911

Hoch, J. M., Eilander, D., Ikeuchi, H., Baart, F., & Winsemius, H. C. (2019). Integrating large-scale hydrology and hydrodynamics for nested flood hazard modelling from the mountains to the coast. *Natural Hazards and Earth System Sciences Discussions*, *March*, 1–18. https://doi.org/10.5194/nhess-2019-75

Hoch, J. M., Haag, A. V., Van Dam, A., Winsemius, H. C., van Beek, L. P. H., & Bierkens, M. F. P. (2017). Assessing the impact of hydrodynamics on large-scale flood wave propagation – A

case study for the Amazon Basin. *Hydrology and Earth System Sciences*, *21*(1), 117–132. https://doi.org/10.5194/hess-21-117-2017

Hoch, J. M., Ikeuchi, H., Eilander, D., Baart, F., Winsemius, H., van Beek, R., & Bierkens, M. (2018). The role of routing - implementing a global routing model into a framework for integrated hydrologic-hydrodynamic inundation modelling. *EGU General Assembly Conference Abstracts*, 8682.

Hoch, J. M., Neal, J. C., Baart, F., van Beek, R., Winsemius, H. C., Bates, P. D., & Bierkens, M. F. P. (2017). GLOFRIM v1.0 - A globally applicable computational framework for integrated hydrological-hydrodynamic modelling. *Geoscientific Model Development Discussions*, *10*, 1–25. https://doi.org/10.5194/gmd-2017-140

Hoch, J. M., van Beek, R., Winsemius, H. C., & Bierkens, M. F. P. (2018). Benchmarking flexible meshes and regular grids for large-scale fluvial inundation modelling. *Advances in Water Resources*, *121*(September), 350–360. https://doi.org/10.1016/j.advwatres.2018.09.003

Hounkpè, J., Diekkrüger, B., Afouda, A. A., & Sintondji, L. O. C. (2019). Land use change increases flood hazard: a multi-modelling approach to assess change in flood characteristics driven by socio-economic land use change scenarios. *Natural Hazards*, *98*(3), 1021–1050.

Huizinga, J., De Moel, H., & Szewczyk, W. (2017). *Global flood depth-damage functions: Methodology and the database with guidelines*. Joint Research Centre (Seville site).

Hunter, N. M., Horritt, M. S., Bates, P. D., Wilson, M. D., & Werner, M. G. F. (2005). An adaptive time step solution for raster-based storage cell modelling of floodplain inundation. *Advances in Water Resources*, *28*(9), 975–991.

ICPR. (n.d.). *Rhine 2020 – Program on the sustainable development of the Rhine*. Retrieved July 10, 2020, from https://www.iksr.org/en/icpr/rhine-2020

Julien, P. Y., Klaassen, G. J., Ten Brinke, W. B. M., & Wilbers, A. W. E. (2002). Case study: Bed resistance of Rhine River during 1998 flood. *Journal of Hydraulic Engineering*, *128*(12), 1042–1050. https://doi.org/10.1061/(ASCE)0733-9429(2002)128:12(1042)

Kramer, N. (2012). *GRADE 2012. Procedure to derive the design hydrograph - Phase 1.*

Lammersen, R., Engel, H., Van de Langemheen, W., & Buiteveld, H. (2002). Impact of river training and retention measures on flood peaks along the Rhine. *Journal of Hydrology*, *267*(1–2), 115–124. https://doi.org/10.1016/S0022-1694(02)00144-0

Leopold, L. B., & Maddock, T. (1953). *The hydraulic geometry of stream channels and some physiographic implications* (Vol. 252). US Government Printing Office.

Merz, B., Kreibich, H., Schwarze, R., & Thieken, A. (2010). Review article "assessment of economic flood damage." *Natural Hazards and Earth System Science*, *10*(8), 1697–1724. https://doi.org/10.5194/nhess-10-1697-2010

Meyer, V., Becker, N., Markantonis, V., Schwarze, R., Van Den Bergh, J. C. J. M., Bouwer, L. M.,

Bubeck, P., Ciavola, P., Genovese, E., Green, C., Hallegatte, S., Kreibich, H., Lequeux, Q., Logar, I., Papyrakis, E., Pfurtscheller, C., Poussin, J., Przyluski, V., Thieken, A. H., & Viavattene, C. (2013). Review article: Assessing the costs of natural hazards-state of the art and knowledge gaps. *Natural Hazards and Earth System Science*, *13*(5), 1351–1373. https://doi.org/10.5194/nhess-13-1351-2013

Meyer, V., Haase, D., & Scheuer, S. (2009). Flood risk assessment in European river basins-concept, methods, and challenges exemplified at the Mulde river. *Integrated Environmental Assessment and Management*, *5*(1), 17–26. https://doi.org/10.1897/IEAM_2008-031.1

Neal, J., Schumann, G., & Bates, P. (2012). A subgrid channel model for simulating river hydraulics and floodplain inundation over large and data sparse areas. *Water Resources Research*, *48*(11), 1–16. https://doi.org/10.1029/2012WR012514

Neal, J., Villanueva, I., Wright, N., Willis, T., Fewtrell, T., & Bates, P. (2012). How much physical complexity is needed to model flood inundation? *Hydrological Processes*, *26*(15), 2264–2282. https://doi.org/10.1002/hyp.8339

NRCS. (2007). Part 630 Hydrology National Engineering Handbook Chapter 16 Hydrographs. In *National Engineering Handbook* (210th–VI–NEH ed.).

Pinter, N., Jemberie, A. A., Remo, J. W. F., Heine, R. A., & Ickes, B. S. (2008). Flood trends and river engineering on the Mississippi River system. *Geophysical Research Letters*, *35*(23), 1–5. https://doi.org/10.1029/2008GL035987

Quoc Thanh, V., Quoc Thanh, V., Roelvink, D., Van Der Wegen, M., Reyns, J., Kernkamp, H., Van Vinh, G., & Thi Phuong Linh, V. (2020). Flooding in the Mekong Delta: The impact of dyke systems on downstream hydrodynamics. *Hydrology and Earth System Sciences*, *24*(1), 189–212. https://doi.org/10.5194/hess-24-189-2020

Sampson, C. C., Smith, A. M., Bates, P. D., Neal, J. C., Alfieri, L., & Freer, J. E. (2015). A high-resolution global flood hazard model. *Water Resources Research*, *51*, 7358–7381. https://doi.org/10.1002/ 2015WR016954

Sanyal, J. (2017). Uncertainty in levee heights and its effect on the spatial pattern of flood hazard in a floodplain. *Hydrological Sciences Journal*, *62*(9), 1483–1498. https://doi.org/10.1080/02626667.2017.1334887

Scussolini, P., Aerts, J. C. J. H., Jongman, B., Bouwer, L. M., Winsemius, H. C., De Moel, H., & Ward, P. J. (2016). FLOPROS: an evolving global database of flood protection standards. *Natural Hazards and Earth System Sciences*, *16*(5), 1049–1061. https://doi.org/10.5194/nhess-16-1049-2016

Shaw, E. M., Beven, K. J., Chappell, N. A., & Lamb, R. (2010). River flow analysis. In *Hydrology in Practice* (4th ed., pp. 235–279). CRC Press LLC.

Soukup, T., Büttner, G., Feranec, J., Hazeu, G., Jaffrain, G., Jindrova, M., Kopecky, M., & Orlitova, E. (2016). CORINE Land Cover 2012 (CLC2012): Analysis and Assessment. *European Landscape Dynamics. CORINE Land Cover Data. CRC/Taylor & Francis, Boca Raton, Florida. Pp*, 93–98.

Straatsma, M., & Huthoff, F. (2011). Uncertainty in 2D hydrodynamic models from errors in roughness parameterization based on aerial images. *Physics and Chemistry of the Earth*, *36*(7–8), 324–334. https://doi.org/10.1016/j.pce.2011.02.009

Sutanudjaja, E. H., van Beek, R., Wanders, N., Wada, Y., Bosmans, J. H. C., Drost, N., Van Der Ent, R. J., De Graaf, I. E. M., Hoch, J. M., De Jong, K., Karssenberg, D., López López, P., Peßenteiner, S., Schmitz, O., Straatsma, M. W., Vannametee, E., Wisser, D., & Bierkens, M. F. P. (2018). PCR-GLOBWB 2: A 5 arcmin global hydrological and water resources model. *Geoscientific Model Development*, *11*(6), 2429–2453. https://doi.org/10.5194/gmd-11-2429-2018

Tiggeloven, T., De Moel, H., Winsemius, H. C., Eilander, D., Erkens, G., Gebremedhin, E., Diaz Loaiza, A., Kuzma, S., Luo, T., Iceland, C., Bouwman, A., Van Huijstee, J., Ligtvoet, W., & Ward, P. J. (2020). Global-scale benefit-cost analysis of coastal flood adaptation to different flood risk drivers using structural measures. *Natural Hazards and Earth System Sciences*, *20*(4), 1025–1044. https://doi.org/10.5194/nhess-20-1025-2020

Tobin, G. A. (1995). the Levee Love Affair: a Stormy Relationship? *JAWRA Journal of the American Water Resources Association*, *31*(3), 359–367. https://doi.org/10.1111/j.1752-1688.1995.tb04025.x

Treby, E. J., Clark, M. J., & Priest, S. J. (2006). Confronting flood risk: Implications for insurance and risk transfer. *Journal of Environmental Management*, *81*(4), 351–359. https://doi.org/10.1016/j.jenvman.2005.11.010

Trigg, M. A., Birch, C. E., Neal, J. C., Bates, P. D., Smith, A., Sampson, C. C., Yamazaki, D., Hirabayashi, Y., Pappenberger, F., Dutra, E., Ward, P. J., Winsemius, H. C., Salamon, P., Dottori, F., Rudari, R., Kappes, M. S., Simpson, A. L., Hadzilacos, G., & Fewtrell, T. J. (2016). The credibility challenge for global fluvial flood risk analysis. *Environmental Research Letters*, *11*(9). https://doi.org/10.1088/1748-9326/11/9/094014

UNDRR. (2015). *Sendai Framework for Disaster Risk Reduction 2015 - 2030*.

van Beek, L. P. H., & Bierkens, M. F. P. (2009). The global hydrological model PCR-GLOBWB: conceptualization, parameterization and verification. *Utrecht University, Utrecht, The Netherlands*, *1*, 25–26.

Van Huijstee, J., Van Bemmel, B., Bouwman, A., & Van Rijn, F. (2018). Towards an Urban Preview: Modelling future urban growth with 2UP. *Background Report, PBL, Den Haag, the Netherlands*.

Van Khanh Triet, N., Viet Dung, N., Fujii, H., Kummu, M., Merz, B., & Apel, H. (2017). Has dyke development in the Vietnamese Mekong Delta shifted flood hazard downstream? *Hydrology and Earth System Sciences*, *21*(8), 3991–4010. https://doi.org/10.5194/hess-21-3991-2017

Ward, P. J., De Moel, H., & Aerts, J. C. J. H. (2011). How are flood risk estimates affected by the choice of return-periods? *Natural Hazards and Earth System Science*, *11*(12), 3181–3195. https://doi.org/10.5194/nhess-11-3181-2011

Ward, P. J., Jongman, B., Aerts, J. C. J. H., Bates, P. D., Botzen, W. J. W., DIaz Loaiza, A., Hallegatte, S., Kind, J. M., Kwadijk, J., Scussolini, P., & Winsemius, H. C. (2017). A global framework for future costs and benefits of river-flood protection in urban areas. *Nature Climate*

Change, *7*(9), 642–646. https://doi.org/10.1038/nclimate3350

Ward, P. J., Jongman, B., Salamon, P., Simpson, A., Bates, P., De Groeve, T., Muis, S., De Perez, E. C., Rudari, R., Trigg, M. A., & Winsemius, H. C. (2015). Usefulness and limitations of global flood risk models. *Nature Climate Change*, *5*(8), 712–715. https://doi.org/10.1038/nclimate2742

Ward, P. J., Jongman, B., Weiland, F. S., Bouwman, A., van Beek, R., Bierkens, M. F. P., Ligtvoet, W., & Winsemius, H. C. (2013). Assessing flood risk at the global scale: Model setup, results, and sensitivity. *Environmental Research Letters*, *8*(4). https://doi.org/10.1088/1748-9326/8/4/044019

Ward, P. J., Winsemius, H. C., Kuzma, S., Bierkens, M. F. P., Bouwman, A., de Moel, H., Loaiza, A. D., Scussolini, P., Sutanudjaja, E. H., van Beek, R., van Bemmel, B., van Huijstee, J., van Rijn, F., & van Wesenbeeck, B. (2020). *Aqueduct Floods Methodology* (Issue January).

Werner, M. G. F., Hunter, N. M., & Bates, P. D. (2005). Identifiability of distributed floodplain roughness values in flood extent estimation. *Journal of Hydrology*, *314*(1–4), 139–157. https://doi.org/10.1016/j.jhydrol.2005.03.012

White, G. F. (1945). Human Adjustment to Floods. Research Paper 29. *Department of Geography , University of Chicago*, 225 pp.

Wing, O. E. J., Bates, P. D., Neal, J. C., Sampson, C. C., Smith, A. M., Quinn, N., Shustikova, I., Domeneghetti, A., Gilles, D. W., Goska, R., & Krajewski, W. F. (2019). A New Automated Method for Improved Flood Defense Representation in Large-Scale Hydraulic Models. *Water Resources Research*, *55*(12), 11007–11034. https://doi.org/10.1029/2019WR025957

Wing, O. E. J., Bates, P. D., Sampson, C. C., Smith, A. M., Johnson, K. A., & Erickson, T. A. (2017). Validation of a 30 m resolution flood hazard model of the conterminous United States. *Water Resources Research*, *53*(9), 7968–7986. https://doi.org/10.1002/2017WR020917

Winsemius, H. C., Van Beek, L. P. H., Jongman, B., Ward, P. J., & Bouwman, A. (2013). A framework for global river flood risk assessments. *Hydrology and Earth System Sciences*, *17*(5), 1871–1892. https://doi.org/10.5194/hess-17-1871-2013

WMI. (2004). *Integrated Flood Management, Concept Paper*. APFM Technical Document No.1, second edition.

Wolman, M. G., & Miller, J. P. (1960). Magnitude and Frequency of Forces in Geomorphic Processes. *The Journal of Geology*, *68*(1), 54–74. https://doi.org/10.1086/626637

Yamazaki, D., Ikeshima, D., Sosa, J., Bates, P. D., Allen, G. H., & Pavelsky, T. M. (2019). MERIT Hydro: A High-Resolution Global Hydrography Map Based on Latest Topography Dataset. *Water Resources Research*, *55*(6), 5053–5073. https://doi.org/10.1029/2019WR024873

Yen, B. C. (1995). Hydraulics and effectiveness of levees for flood control. *Hydrometeorology, Impacts and Management of Extreme Floods*, *November*.

Appendix

A. Design hydrographs for the single event-simulations

The task of deriving a series of discharge profiles to use as input for Method B is contingent upon the available data and the necessity to make a few assumptions on the shape of the hydrographs. In addition, the hydrographs must reflect the extreme return period flows at the inlet of the hydrodynamic domain for the series of 2, 5, 10, 25, 50, 100, 250, 500 and 1000 years. Ideally, design hydrographs could be derived empirically from a long-term series of measured or modelled flows though statistical analysis; for instance, this procedure has been developed in the GRADE project for the Rhine and Meuse catchments (de Wit & Buishand, 2007; Kramer, 2012). However, this requires a sufficiently large sample of discharge data to produce a significant mean for the largest return periods. For example, for GRADE a 20000 years-long simulation was used, compared to the 40 years used in this study. In the hindsight of this, a simpler approach such as the Soil Conservation Service (SCS) synthetic hydrograph method is more favourable for this study (NRCS, 2007). This is based on a series of empirical relationships based on the catchment characteristics and the typical response hydrographs, which aim to reproduce a realistic curve shape independently of the availability of rainfall-runoff observations and of a design storm. As starting point, the Base simulation at Bonn is analysed to retrieve the 2, 5, 10, 25, 50, 100, 250, 500, 1000 years return period discharges using a Gumbel estimation, providing the values of peak discharge $Q_p\ (m^3/s)$ for the hydrographs. Then, Giandotti's formula is used to retrieve the time of concentration for the catchment at Bonn:

$$t_C = \frac{4\sqrt{S} + 1{,}5L}{0.8\sqrt{H_m - h_0}} \qquad [A.1]$$

where t_C (days) is the time of concentration, S (km2) is the surface of the catchment upstream of Bonn, L (km) is the length of the Rhine at Bonn, H_m (m) is the average catchment elevation and h_0 (m) is the elevation at Bonn; this yields an estimate of ~ 159 hours. The SCS method assumes that a relationship exists between t_C and the time to peak t_p of the type:

$$t_p = \frac{\Delta D}{2} + L \qquad [A.2]$$

where ΔD is the duration of the unit excess rainfall and L is the lag time for the catchment, respectively defined by:

$$\Delta D = 0.133\, t_C\,, \quad L = 0.6\, t_C \qquad [A.3]$$

Using this set of equations, the typical gamma equation can be invoked to define the instantaneous discharge $Q\ (m^3/s)$ for each time interval t of the hydrograph with respect to the reference peak discharge:

$$\frac{Q}{Q_p} = e^m \left(\frac{t}{t_p}\right)^m \left[e^{-m\left(\frac{t}{t_p}\right)}\right] \qquad [A.4]$$

where m is a unitless factor that depends on the peak rate factor (PRF) of the catchment. The PRF classifies the response of the catchment according to the overall flatness or steepness of the slopes (NRCS, 2007). For our case, a standard value of $m = 3.7\ [-]$ is used to avoid characterising the catchment in either direction. This procedure yields the set of hydrographs showcased in Figure A.1. As can be noticed, the method assumes that the rising limb of the hydrograph sets off from an initial null discharge, and that after the event this condition is restored, as the falling limb returns to this level. Of course, this hypothesis is unrealistic for a real channel, as it is the fact that each discharge peak will occur at the same time. In reality, higher peaks will be generally translated at a later time as result of the longer duration needed for a similar rainfall event.

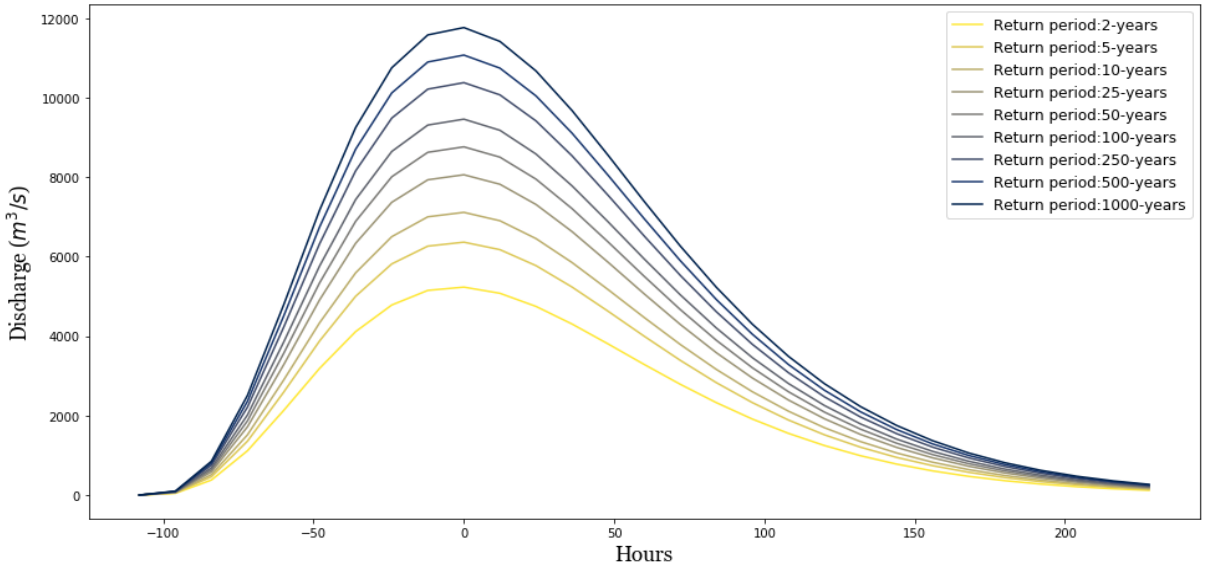

Figure A.4: Series of hydrograph obtained through the SCS method for each return period.

To provide a comparison, an efficiently simplified variation of the methodology of Kramer (2012) is used to derive the 2-years return period hydrograph based on the series of hydrographs obtained with the model at Bonn. The relatively short time span of the dataset imposes a first variation from the original procedure, in that a peak over threshold (POT) system is used to individuate the series of discharge profiles needed. This is because the number of hydrologically relevant events in the series is constrained and does not provide a large enough sample for each return period class; the POT yields information on the extremes of the series and has been previously applied to design empirically-derived hydrographs (Clerc et al., 2003). The 2-years return discharge determines the baseline for the POT selection, providing a sample of 41 peaks. This discharge value provides a good trade-off between statistical significance (in the number of peaks individuated) and representativeness of extreme events. Using a linear proportion between the peak values of each hydrograph and the peak value of the lowest hydrograph, all profiles can be scaled to the same maximum. This set of curves is vertically averaged (on the basis of daily time steps) to obtain a single curve. The 41-peaks cluster obtained with the 2-years POT leads to consider a large range of discharge values for the peaks. This could make the series diverge from the assumption of shape invariance (Clerc et al., 2003). Figure A.2 shows how, by choosing increasing values for the return period of the discharge in the POT sampling, the shape of the resulting hydrograph becomes narrower and

sharper. The problem with this is that the characteristic shape for a certain discharge is lost in the averaging procedure. Kramer (2012) bypasses this issue by selecting small ranges of discharge values that produce a number of classes, each with its characteristic profile; however, the limited number of peaks available for this study does not consent to use the same approach. One additional condition imposed here in the selection of the POT is that at the start and end of the event the discharge value has to be 80% of that at the peak of the curve, leaving a total of 14 events. This is to partially eliminate the shoulders which could flatten the peak profile and to obtain a clean-cut curve. Vertical averaging of the profiles is used as opposed to horizontal averaging since the former is judged better at preserving the overall flood volume (Kramer, 2012). After obtaining the mean value for the curve, the error intervals are obtained at each time step based on a confidence of 95%; this yields the profile in Figure A.3.

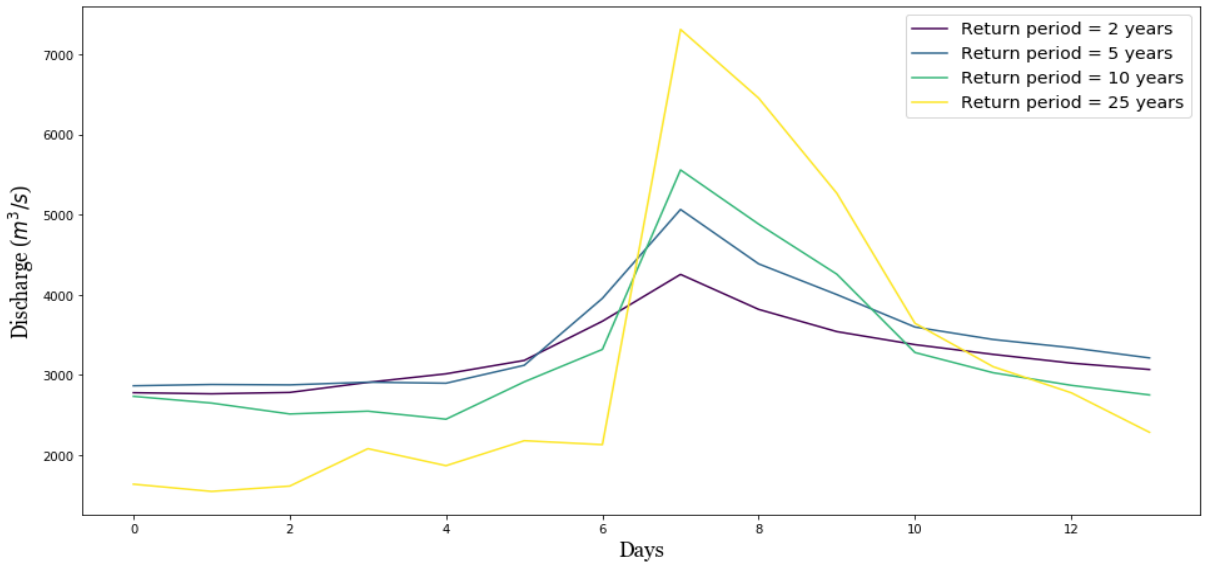

Figure A.5: scaled and vertically averaged hydrographs obtained for the POT discharge values corresponding to 2, 5, 10, 50 years return period discharges at Bonn.

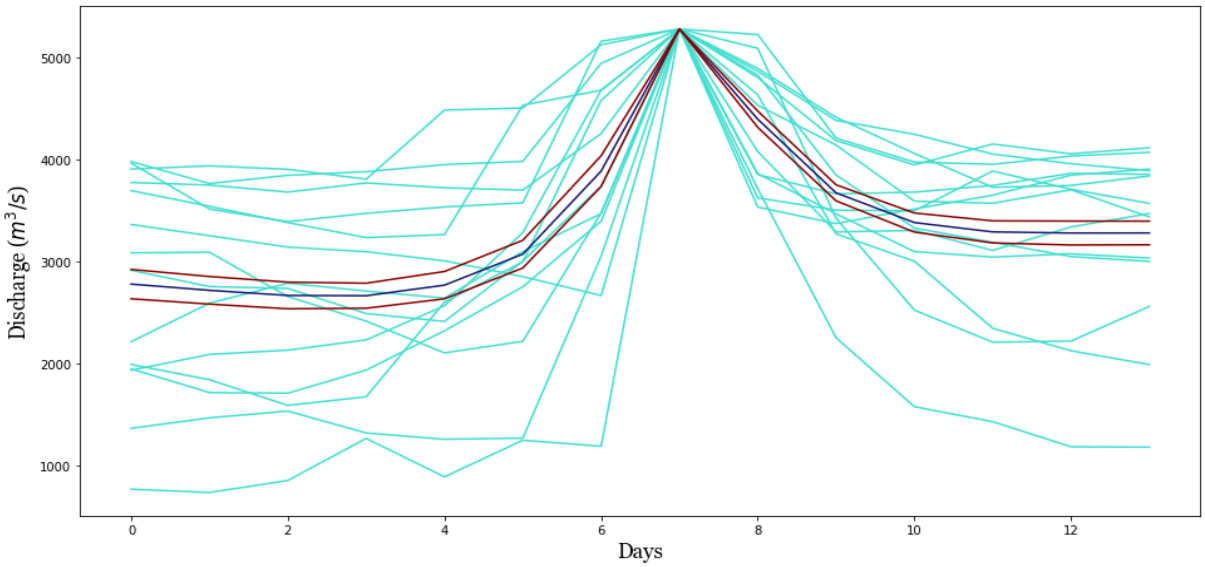

Figure A.6: 2-years return period event hydrograph. The upper and lower confidence bounds are represented in red, while the population of events used to delineate the hydrograph is represented in light blue.

As expected, the hydrograph derived by averaging of the time series differs significantly on the offset value of the rising limb, which corresponds to roughly 3000 m3/s. As can be observed by a direct comparison of the two hydrograph curves in Figure A.4, this results for the SCS method in a significant underestimation of the total area under the curve and therefore of the total volume of the water during the event.

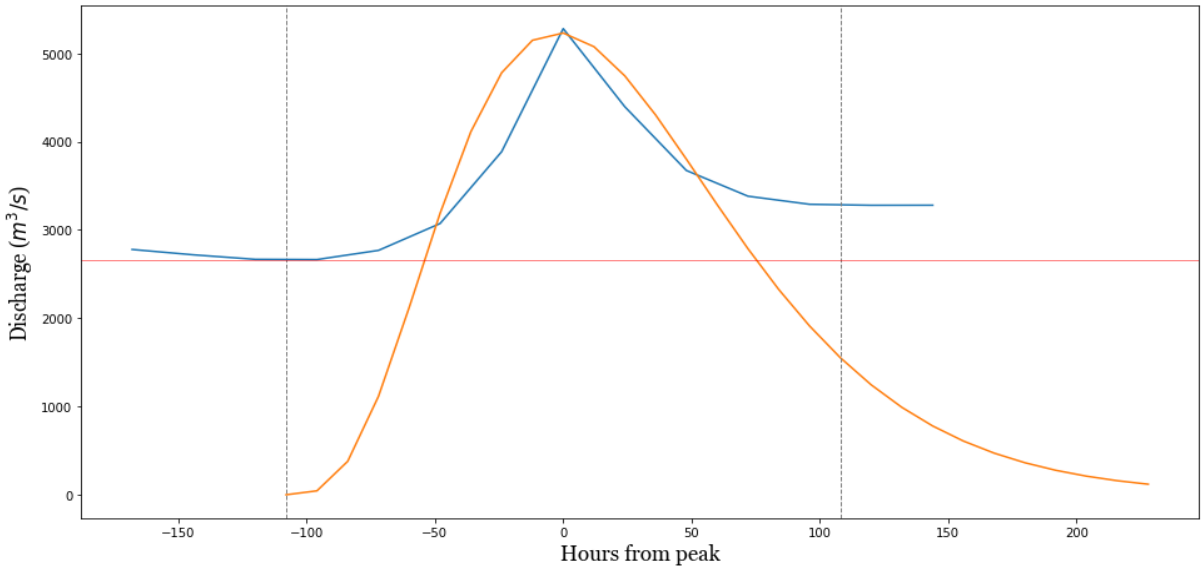

Figure A.7: Overlaid image of the SCS hydrograph and the empirical hydrograph for the 2-years return period discharge.

To compensate for this, the hydrographs derived for the study are the product of a combination of these two methods. By doing this, the aim is to make up for the absence of long-term discharge data

needed for the full empirical approach, and for the underestimation of the event flow volume of the SCS method. Therefore, the profiles obtained with the SCS method are overlaid on the baseline of the empirical 2-years hydrograph, obtaining the peaks shown in Figure A.5. When considering the limitations in representativeness of real events characteristic of this method it should be born in mind that, rather than between the different return period events for the same scenario, the objective of study is a cross-scenario comparison. In light of this, the fundamental features of the derived curves are the accuracy in depicting the peak discharge and a realistic shape. Both these conditions are respected.

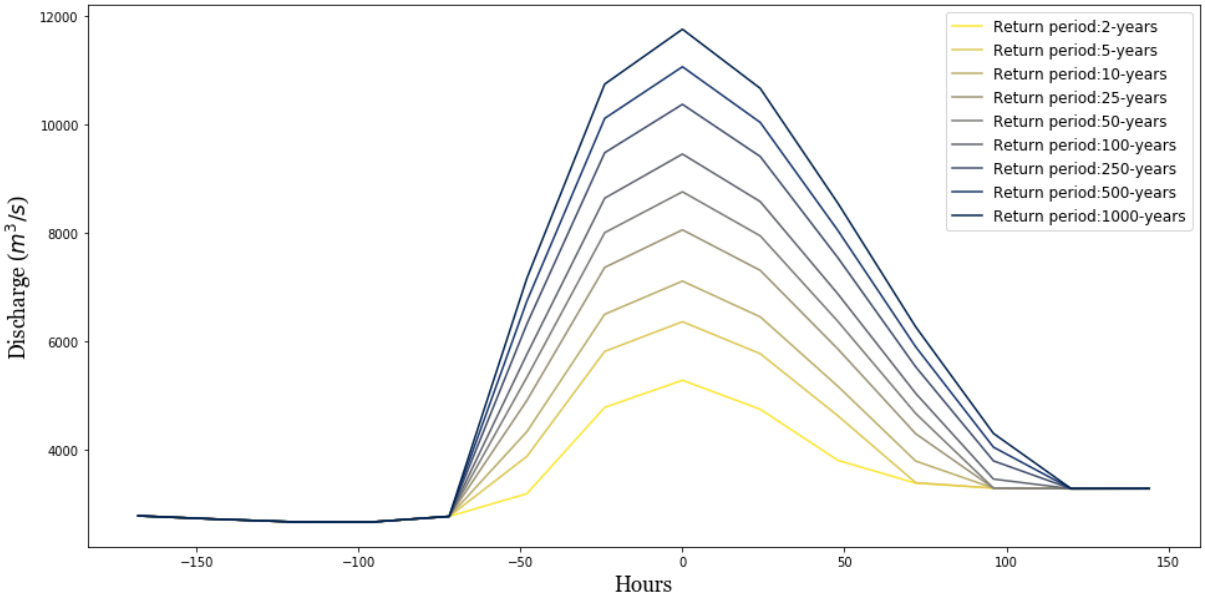

Figure A.8: Set of hydrographs from the combination of the two methods, used as input in the model.

B. Depth-damage functions

The values used for the vulnerability functions are taken from the data of Huizinga et al. (2017) (Table B.1). The depth-damage functions are plotted by occupancy type in Figure B.1.

Table B.3: Values reported for the vulnerability functions used, relative to the occupancy types.

Occupancy types	**Residential**	**Industrial**	**Commercial**
Flood depth (m)		Damage (%)	
0	0	0	0
0.1	0,074	0,063	0,069
0.5	0,368	0,317	0,343
1	0,534	0,506	0,527
1.5	0,648	0,623	0,645
2	0,746	0,710	0,754
2.5	0,807	0,770	0,809
3	0,867	0,830	0,864
3.5	0,898	0,877	0,893
4	0,929	0,923	0,923
4.5	0,951	0,950	0,945
5	0,972	0,977	0,968
≥ 5	1,000	1,000	1,000

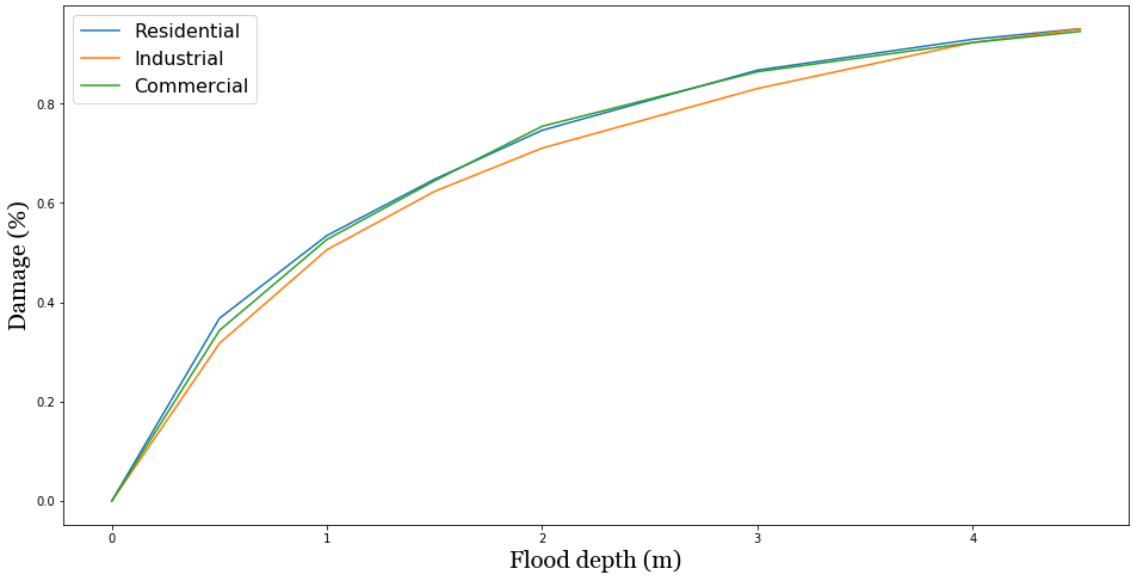

Figure B.1: Plot of the vulnerability functions used for the three occupancy types.

C. Uncertainty and errors on the Gumbel distribution

To evaluate the goodness-of-fit for the Gumbel analysis on the annual maxima of the series, the Gumbel distribution equation (Eq. 3.5) can be rearranged as:

$$\frac{T_r}{T_r - 1} = F(Q) = exp\left[-exp\left(-\frac{Q-a}{b}\right)\right] \qquad [C.1]$$

Where $F(Q)$ is the frequency of exceedance of a discharge value, and a, b are the 'moments' of the equation, respectively dependant on the mean and standard deviation of the annual maximum values series (Shaw et al., 2010). This equation can be linearized by taking the double logarithm of the frequency, or standard Gumbel variate:

$$ln\{-ln[F(Q)]\} = \frac{a-Q}{b} \qquad [C.2]$$

at this point, the coefficient of determination R^2 can be invoked to establish the goodness-of-fit for the Gumbel linearized function by comparing it with the annual maxima obtained through modelling. These values are plotted according to their position r in a ranking of discharge magnitude of the total number of maxima N, and by associating a frequency value using the Gringorten formula (Shaw et al., 2010):

$$F(X) = 1 - \frac{r - 0.44}{N + 0.12} \qquad [C.3]$$

From these values, the Gumbel variate can be retrieved for every point in the sample. Hence, the coefficient of determination is calculated from:

$$R^2 = 1 - \frac{SS_{Res}}{SS_{Tot}} \qquad [C.4]$$

where SS_{Res} is the residual sum of squares and SS_{Tot} is the total sum of squares. These can be computed respectively by:

$$SS_{Res} = \sum_i (y_i - f_i)^2 \qquad and \qquad SS_{Tot} = \sum_i (y_i - \bar{y})^2 \qquad [C.5]$$

with y_i sampled value for a certain Gumbel variate, f_i interpolated value and $\bar{y}$ mean value

The confidence bounds on the extrapolation can be computed, considering a confidence interval of 95%, using the equations:

$$Err\left(\widehat{D_r}\right) = \pm\, t_{\alpha,\vartheta} \sqrt{\left\{\frac{s_D}{\sqrt{N}}[1 + 1.14K(T)^2]\right\}}, \qquad K(T) = -\frac{\sqrt{6}}{\pi} * \left\{0.5772 + ln\left[ln\left(\frac{T_r}{T_r - 1}\right)\right]\right\} \qquad [C.6]$$

where $t_{\alpha,\vartheta}$ is the relative Student's t and $Err\left(\widehat{D_r}\right)$ is the error on the flood depth for a certain return period and all other parameters were previously defined.

D. Flood hazard results

Hydrograph profiles at Lobith

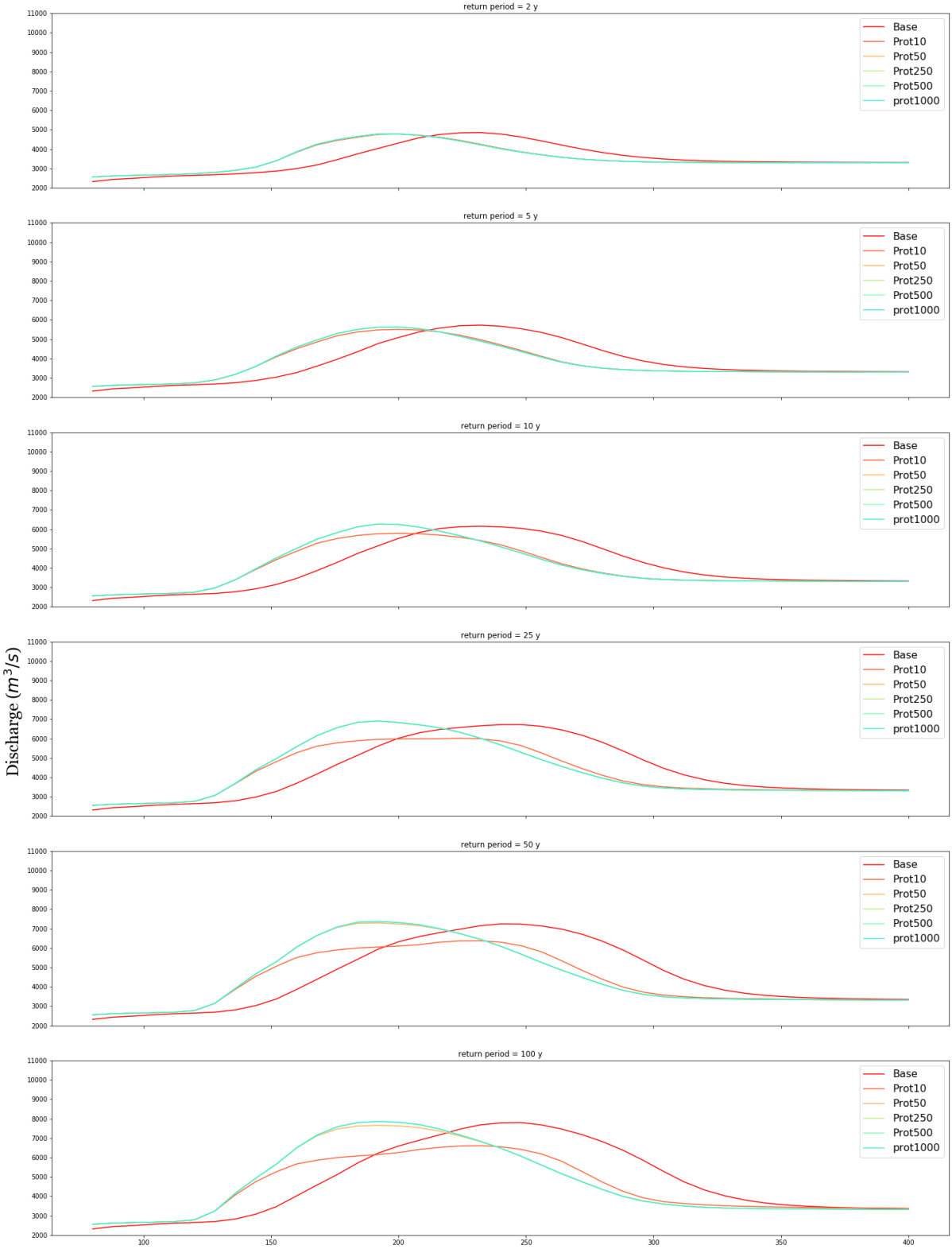

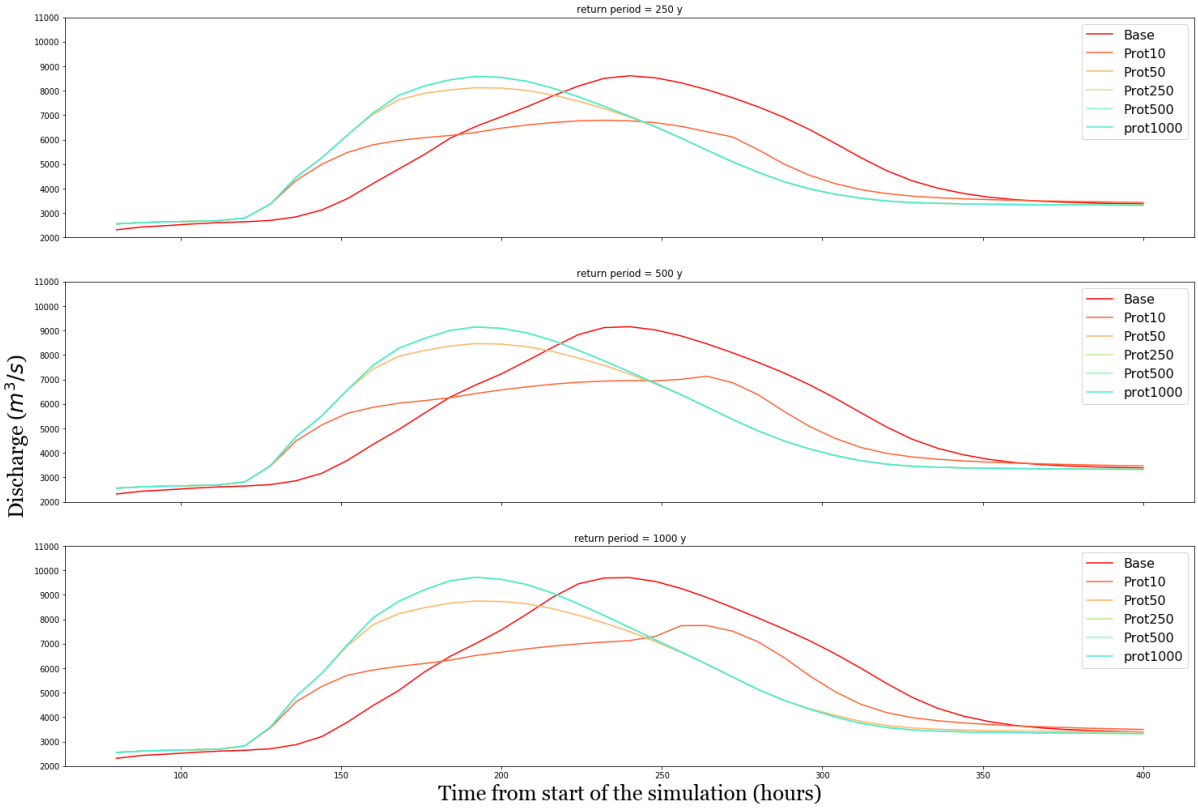

Figure D.1: Comparison of the scenarios Base to Prot1000 at Lobith based on the discharge profile. In each plot, a different return period event is considered.

Comparison of the flood extent between the two methods

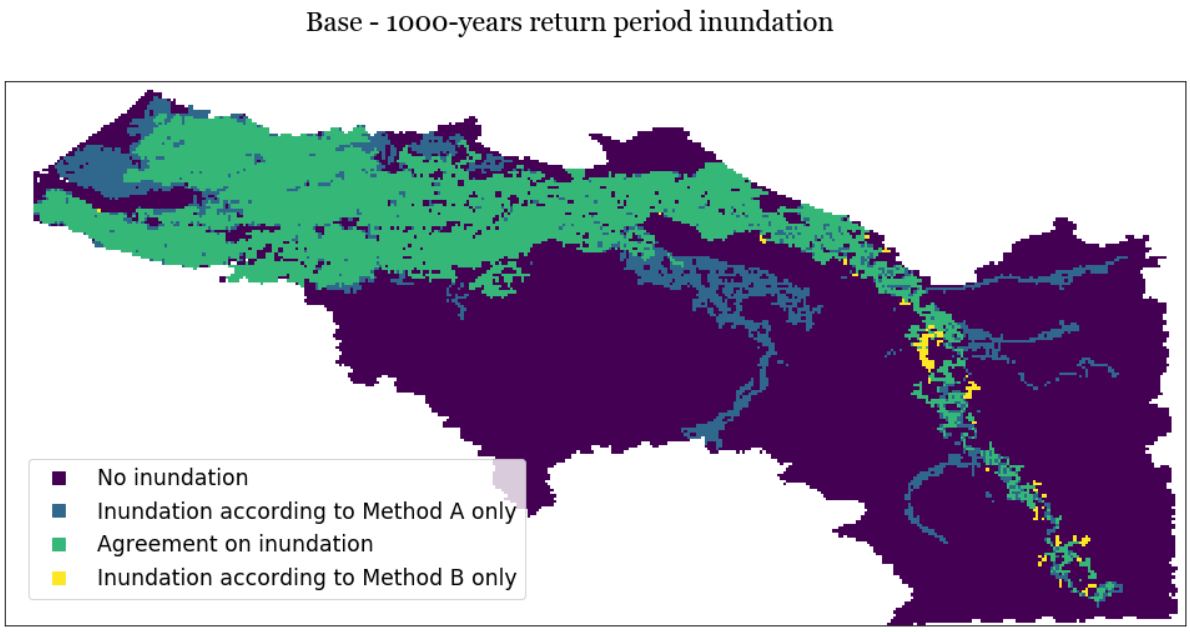

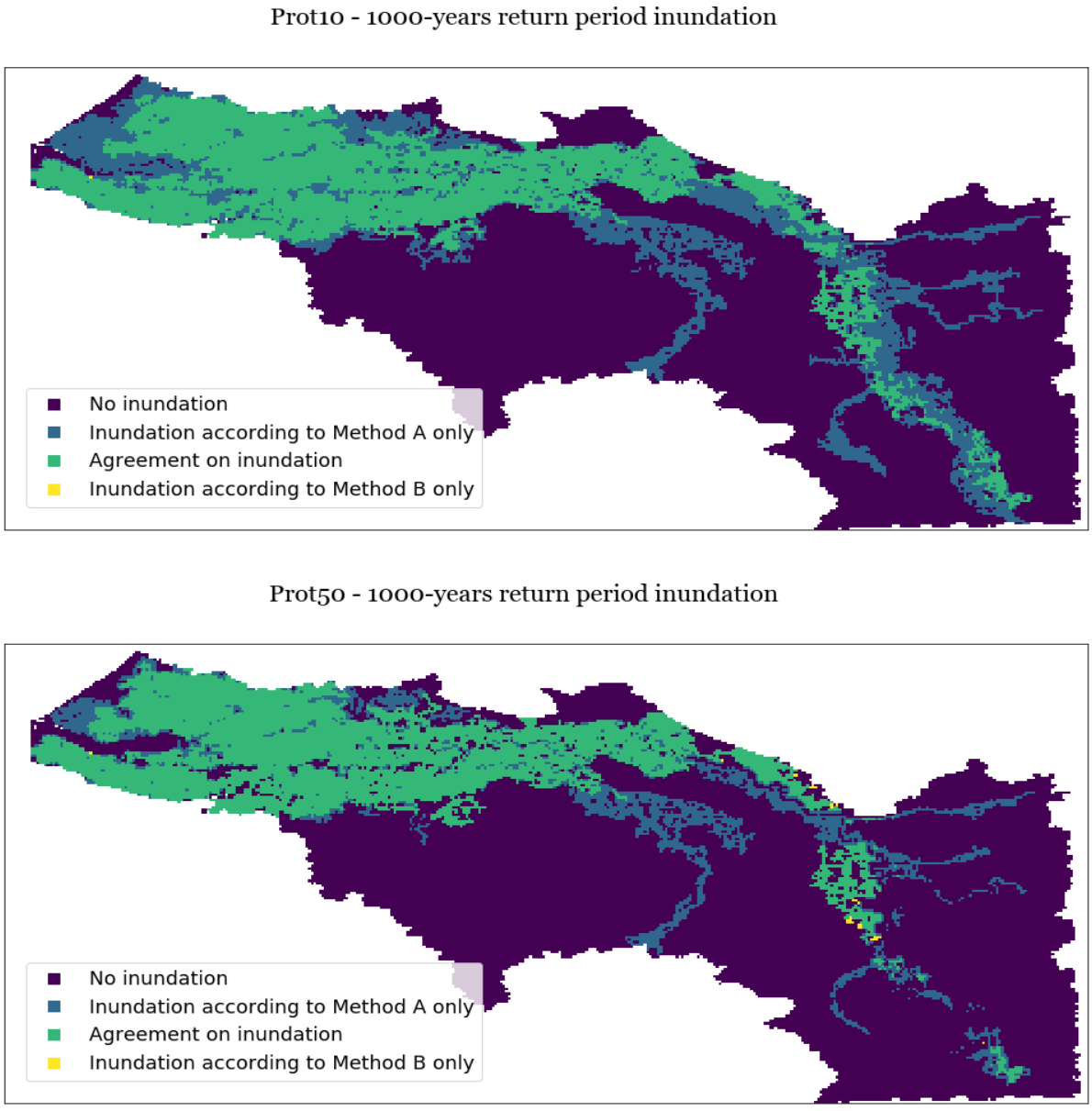

Figure D.2: Comparison of the 1000-year return period inundation extent modelled using method A (statistical extrapolation) and method B (from the design hydrographs). Each figure corresponds to a protection scenario. Scenarios Prot250/500/1000 are given in the text.